



# Forward GEM Tracker (FGT)

A

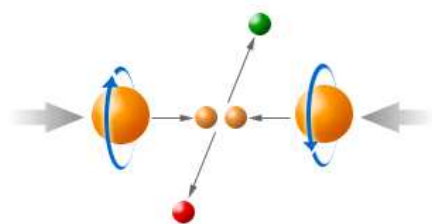
Forward Tracking Upgrade Proposal

(DRAFT - Version 2)

for the

STAR experiment

January 2007



# **Forward GEM Tracker (FGT)**

**A**

## **Forward Tracking Upgrade Proposal for the STAR experiment**

H. Spinka, D. Underwood  
**Argonne National Laboratory, Argonne, IL, USA**

J. Balewski, W. Jacobs, S. Vigdor, J. Sowinski, S. Wissink  
**Indiana University Cyclotron Facility, Bloomington, IN, USA**

H.G. Ritter, E. Sichtermann  
**Lawrence Berkeley National Laboratory, Berkley, CA, USA**

R. Fatemi, D. Hasell, J. Kelsey, K. Dow, M. Miller, R. Milner, M. Plesko,  
R. Redwine, F. Simon, B. Surrow, G. van Nieuwenhuizen  
**Massachusetts Institute of Technology, Cambridge, MA, USA**

D.P. Grosnick, D.D. Koetke, R.W. Manweiler, T.D.S. Stanislaus  
**Valparaiso University, Valparaiso, IN, USA**

R. Majka, N. Smirnov  
**Yale University, New Haven, CT, USA**

# Contents

<b>1</b>	<b>Executive summary</b>	<b>1</b>
<b>2</b>	<b>Physics program</b>	<b>4</b>
2.1	Polarized Structure Function Physics . . . . .	4
2.2	The RHIC Spin program . . . . .	4
2.3	W physics . . . . .	6
<b>3</b>	<b>Layout and simulation results</b>	<b>16</b>
3.1	Overview . . . . .	16
3.2	Requirements . . . . .	18
3.3	Simulation results . . . . .	22
<b>4</b>	<b>Technical realization</b>	<b>38</b>
4.1	Overview . . . . .	38
4.2	GEM Technology . . . . .	38
4.3	GEM R&D . . . . .	40
4.4	Technical sub-systems . . . . .	46

## List of Figures

1	Production of a $W^+$ in a $\vec{p}p$ collision, at lowest order. . . . .	8
2	W kinematic coverage of $x_1$ and $x_2$ for different values of $y$ . . . . .	9
3	Helicity configuration of $W^-$ and $W^+$ production. . . . .	10
4	Leptonic $p_T$ cross section for the $W^+$ and $W^-$ case. . . . .	11
5	Leptonic $p_T$ cross section for the $W^+$ and $W^-$ case. . . . .	12
6	The sensitivity to different underlying quark and anti-quark distributions. . . . .	13
7	The ratio $R_W = (d\sigma(W^-)/dy)/(d\sigma(W^+)/dy)$ for unpolarized $pp$ collisions at RHIC. . . . .	14
8	Layout of the Forward GEM Tracker. . . . .	17
9	Comparison of RHICBOS and PYTHIA simulation results. . . . .	19
10	Sagitta (mm) as a function of $p_T$ and $\eta$ . . . . .	20
11	Transverse momentum and total energy of electrons (left column) and positrons (right column) in W events from Pythia in the STAR EEMC acceptance region. . . . .	21
12	Ratio of the energy deposited in various STAR EEMC calorimeter elements to the total energy. . . . .	23
13	$p_T$ distribution for PYTHIA background and signal events. . . . .	24
14	PYTHIA prediction of hadron $p_T$ for $\sqrt{s} = 500$ GeV W production in p+p collisions. . . . .	25
15	PYTHIA prediction of hadron multiplicity spectra for $\sqrt{s} = 500$ GeV W production in p+p collisions. . . . .	26
16	Position resolution for log-weighting method of STAR EEMC shower-maximum strip information . . . . .	28
17	. . . . .	29
18	. . . . .	30
19	. . . . .	31
20	Charge sign discrimination probability for TPC only . . . . .	32
21	Track reconstruction efficiency and charge discrimination probability - Set 1 . . . . .	33
22	Track reconstruction efficiency and charge discrimination probability - Set 2 . . . . .	35
23	Track reconstruction efficiency and charge discrimination probability - Set 3 . . . . .	36
24	Electron microscope picture of a GEM foil and cross section view through one hole. . . . .	39

25	Simulated electrical field inside a GEM hole. . . . .	40
26	Distribution of inner hole diameter. . . . .	41
27	Bottom and top view of the prototype triple-GEM chambers. .	42
28	Exploded view of a prototype triple-GEM chamber indicating the location of various chamber elements. . . . .	43
29	$^{55}\text{Fe}$ spectrum with a CERN triple GEM test detector . . . . .	44
30	$^{55}\text{Fe}$ spectrum with a Tech-Etch triple GEM test detector . . .	44
31	Gain map of Tech-Etch triple GEM . . . . .	45
32	Picture of the APV25-S1 die. . . . .	46
33	Schematic drawing of readout structure . . . . .	48
34	Sketch of the APV25 chip readout system and STAR DAQ integration. . . . .	50
35	RPC event in APV25 . . . . .	51

## List of Tables

1	Helix hit parameters. . . . .	27
2	Simulation configurations. . . . .	34

## 1 Executive summary

The STAR collaboration is preparing a challenging tracking detector upgrade program to further investigate fundamental properties of the new state of strongly interacting matter produced in relativistic-heavy ion collisions at RHIC and to provide fundamental studies of the nucleon spin structure and dynamics in high-energy polarized proton-proton collisions at RHIC.

A future core goal of the STAR scientific spin program is to carry out measurements to determine the flavor-dependence ( $\Delta\bar{u}$  versus  $\Delta\bar{d}$ ) of the sea quark polarization, and thereby examining the mechanism for producing the sea in a proton. Those polarized distribution functions are only weakly constrained by polarized fixed-target DIS experiments [1]. This will be probed using parity-violating  $W$  production and decay. The method for extracting spin-dependent quark distributions based on the reconstruction of the single-longitudinal spin asymmetry as a function of the  $W$  rapidity is not possible since reconstruction of the  $W$  is only possible with a hermetic detector. However it has been shown that most of the sensitivity to anti-quark polarizations is preserved in the leptonic observables. The theoretical framework on the measurement of the single-longitudinal spin asymmetry as a function of the leptonic rapidity has been presented in [2]. Reliable predictions are provided based on resummation calculations. These calculations have been incorporated in a Monte-Carlo program called RHICBOS. These concepts have been used extensively for the  $W$  mass measurement at the Tevatron. The production of  $W^{-(+)}$  bosons provides an ideal tool to study the spin-flavor structure of the proton.  $W^{-(+)}$  bosons are produced in  $\bar{u}+d(d+\bar{u})$  collisions and can be detected through their leptonic decays into an electron and a neutrino, or the corresponding anti-particles. Forward scattered  $e^{-(+)}$  tagged in the STAR Endcap ElectroMagnetic calorimeter (EEMC) ( $1 < \eta < 2$ ) off the incoming polarized proton beam moving toward (away) from the STAR EEMC, yield a purity for  $W^{-(+)}$  coming from  $\bar{u} + d$  ( $d + \bar{u}$ ) quarks of about 98% (75%) [3]. The separation of  $e^{-(+)}$  from hadronic background will be important and therefore the full exploitation of the STAR EEMC with its intrinsic means for  $e/h$  separation (pre-shower and post-shower readout system) will be crucial. The discrimination of  $\bar{u}+d(d+\bar{u})$  quark combinations requires distinguishing between high  $p_T$   $e^{-(+)}$  through their opposite charge sign which in turn requires precise tracking information. The resolution of the STAR Time-Projection Chamber (TPC) deteriorates rapidly beyond  $|\eta| > 1$ . It does not permit charge discrimination for high  $p_T$  tracks. An upgrade of the

STAR forward tracking system is needed to provide the required tracking precision for charge sign discrimination. The forward tracking system would consist of six triple-GEM detectors with two dimensional readout arranged in disks along the beam axis, referred to as the Forward GEM Tracker (FGT). The forward tracking components provide precision tracking in the range of  $1 < \eta < 2$ , giving charge sign discrimination for leptonic decays of  $W$  bosons. The charge sign determination of forward scattered  $e^{-(+)}$ , tagged in the STAR EEMC in polarized proton-proton collisions is the main motivation for the STAR Forward Tracking Upgrade.

Several options have been studied based on disk and barrel arrangements. The proposed configuration based on six triple-GEM disk detectors addresses several issues such as optimized acceptance taking into account the  $Z$  vertex distribution with a Gaussian sigma of about 30 cm. It has been shown that a disk configuration is optimal in terms of acceptance in comparison to a barrel configuration in particular at large  $\eta$ . The proposed configuration provides a rather cost effective solution based only on GEM technology. The usage of additional silicon disks at smaller radii as originally anticipated does not yield an improvement in performance and is no longer considered. GEM technology is widely employed by current and future experiments in nuclear and particle physics. A SBIR proposal (Phase 1 and Phase 2) has been approved and is the basis for the industrial production of GEM foils to be used for the forward GEM tracking system. The readout system for both the intermediate (IST) and forward (FGT) tracking systems are based on the APV25-S1 readout chip which has been extensively tested for the CMS silicon tracker and is also used by the COMPASS triple-GEM tracking stations. A common chip readout system will significantly simplify the design of the overall readout system for the integrated tracking upgrade. The proposed configuration is based on light-weight materials to limit the amount of dead material in the forward direction. It provides also the possibility to decouple the inner and forward tracking system from a mechanical perspective. In summary, the charge-sign discrimination of high- $p_T$   $e^{-(+)}$  to distinguish  $W^{-(+)}$  bosons is based on using a beam line constraint, precise hit information from six triple-GEM disks, hits at forward  $\eta$  from the TPC and the electromagnetic-cluster hit information from the shower-maximum detector of the STAR EEMC.

It should be stressed that the integrated tracking upgrade for STAR based on well-established, intrinsically fast detector and readout elements, will provide a significant improvement of the existing STAR tracking system, in

particular for the expected high luminosity operation at RHIC.

## 2 Physics program

### 2.1 Polarized Structure Function Physics

The 1988 publication of small Bjorken- $x$  measurements of the inclusive spin structure function  $g_1^p$  by the European Muon Collaboration marks a major surge of interest in the spin structure of the nucleon.

In polarized DIS experiments a polarized photon with virtuality  $Q^2$  probes the charged substructure of the polarized nucleon, composed of quarks, gluons, and anti-quarks. Among the most important results from the polarized DIS experiments are the confirmation of the Bjorken Sum rule and the smallness of the polarized cross-section. The Bjorken Sum rule relates the difference of the moments of the polarized up and down (anti-)quark distributions to the coupling in neutron beta decay, and is a tenet of QCD. The smallness of the spin structure function, or the spin-dependent cross section, means that the combined (anti-)quark spins carry only a small fraction of about 20% of the nucleon spin. This result is in striking contrast with predictions from constituent quark models, which successfully describe hadron magnetic moments and spectroscopy, and is often referred to as the ‘proton spin crisis’.

Soon after its discovery it was recognized that gluon helicity could well be an important contributor to the nucleon spin. QCD predicts that gluon helicity rises logarithmically with  $Q^2$ , a remarkable pattern related to the so-called axial anomaly. It has been conjectured that gluon helicity could ‘shield’ the quark helicity and thus explain the observed smallness of the polarized structure function.

Precise measurement of gluon polarization in the nucleon became a worldwide quest, as did the delineation of the (anti-)quark spin contribution by flavor. In spite of the large body of DIS data and the promise from new and ever better experiments, polarized DIS measurements have important limitations. In particular, they do not directly provide information about the gluon and anti-quark distributions. Hence, the interest in polarized hard-hadronic processes which could offer new physics insight, complementary to DIS.

### 2.2 The RHIC Spin program

The nucleon spin physics program at the Relativistic Heavy Ion Collider (RHIC) has largely been motivated by the unexpected and nonintuitive re-

sults from polarized lepton-nucleon deep-inelastic scattering (DIS) experiments.

The first polarized proton run at RHIC at Brookhaven National Laboratory from December 2001 until January 2002 marks the start of a multi-year experimental program which aims to address a variety of topics related to the nature of the proton spin such as

- the gluon spin contribution to the proton spin, and
- the quark and anti-quark polarization in the proton.

Other important aspects concern the transversity distributions in the proton, the spin dependence of fundamental interactions, the spin dependence of fragmentation, and the spin dependence of elastic polarized proton scattering. A review of the RHIC spin program may be found in [4].

The RHIC facility is the first polarized collider, providing collisions of transverse or longitudinal polarized proton beams at a center-of-mass energy of  $\sqrt{s} = 200$  GeV and in the future of  $\sqrt{s} = 500$  GeV. The STAR spin physics program has profited enormously from the steady improvement and development of the RHIC polarized proton-proton collider facility in terms of polarization and luminosity. The performance of the most recent run in 2006 (Run 6) is very encouraging with an average polarization of 60% and a delivered luminosity per day of approximately  $1 \text{ pb}^{-1}$  at  $\sqrt{s} = 200$  GeV. This is to be compared with the design performance of 70% in beam polarization and a daily delivered luminosity of approximately  $3 \text{ pb}^{-1}$  at  $\sqrt{s} = 200$  GeV. Several improvements along with the required subsequent development of the RHIC facility are expected to yield the anticipated design luminosity of  $0.8(2.0) \cdot 10^{32} \text{ cm}^{-2} \text{ s}^{-1}$  at 200 GeV (500 GeV) and a beam polarization of 70%.

During the period of 2004-2009, the major physics goal of the STAR spin program at RHIC is a comprehensive study of the proton's spin structure and dynamics, in particular the nature of the QCD sea, using polarized protons. The centerpiece of this program is the measurement of the gluon contribution to the proton spin using various probes involving final-state jets such as inclusive jet production, di-jet production, prompt photon production and heavy-flavor production in the collision of longitudinal polarized protons.

Among the first results at RHIC are measurements of the unpolarized, or spin-averaged, cross sections for inclusive neutral pion and inclusive jet production. The spin-averaged cross sections at large transverse momenta are

well-described over several orders of magnitude with perturbative QCD calculations at next-to-leading order using unpolarized quark and gluon distribution functions (and fragmentation functions). The agreement of predicted and observed production cross section helps establish the interpretation of polarized measurements at RHIC in the standard factorized framework of perturbative QCD as a reliable path to further advance our knowledge of the nucleon spin structure and the gluon polarization in particular.

At a center of mass energy of 200 GeV the program focuses on the determination of the gluon contribution to the proton spin as well as the study of transverse phenomena. In the future 500 GeV era of RHIC the study of the flavor dependence of sea anti-quark polarization in the proton through the production of W bosons is possible. RHIC has successfully accelerated, stored, and collided protons at  $\sqrt{s} = 410$  GeV as part of its development program in the year 2005. This, together with measured survival of proton polarization, bodes well for these future measurements.

### 2.3 W physics

Measurements in polarized DIS [5], when combined with information from baryon octet  $\beta$ -decays [6], show that the total quark-plus-antiquark contribution to the proton's spin, summed over all flavors, is surprisingly small. In the standard interpretation of the  $\beta$ -decays [6], this finding is equivalent to evidence for a large negative polarization of strange quarks in the proton, which makes it likely that also the  $SU(2)$  ( $u, d$ ) sea is strongly negatively polarized. This view is corroborated by the fact that in this analysis the spin carried, for example, by  $u$  quarks comes out much smaller than generally expected in quark models [6], implying that a sizeable negative  $u$ -sea polarization partly compensates that of the valence  $u$  quarks. Alternative treatments of the information from  $\beta$ -decays [7, 8], when combined with the DIS results, also directly yield large negative  $\bar{u}$  and  $\bar{d}$  polarizations. Inclusive DIS (through  $\gamma^*$  exchange) itself is sensitive to the combined contributions of quarks and antiquarks of each flavor but cannot provide information on the polarized quark and antiquark densities separately. Directly measuring the individual polarized antiquark distributions is therefore an exciting task and will also help to clarify the overall picture concerning DIS and the  $\beta$ -decays.

Further motivation for dedicated measurements of antiquark densities comes from unpolarized physics. Experiments in recent years have shown [9, 10, 11] a strong breaking of  $SU(2)$  symmetry in the antiquark sea, with the

ratio  $\bar{d}(x)/\bar{u}(x)$  rising to 1.6 or higher. It is very attractive to learn whether the polarization of  $\bar{u}$  and  $\bar{d}$  is large and asymmetric as well. Within the chiral quark soliton model based on a  $1/N_c$  expansion, it is expected that the polarized flavor asymmetry,  $\Delta\bar{u} - \Delta\bar{d}$ , is larger than the experimentally established flavor asymmetry in the unpolarized sector [12]. A measurement of the polarized flavor asymmetry will shed light into the underlying mechanism responsible for the expected polarized flavor asymmetry. RHIC experiments will measure the  $\bar{d}/\bar{u}$  unpolarized ratio and the  $\bar{u}$  and  $\bar{d}$  polarizations separately.

Semi-inclusive DIS measurements [13] are one approach to achieving a separation of quark and antiquark densities. This method combines information from proton and neutron (or deuteron) targets and uses correlations in the fragmentation process between the type of leading hadron and the flavor of its parton progenitor, expressed by fragmentation functions. The dependence on the details of the fragmentation process limits the accuracy of this method. At RHIC the polarization of the  $u, \bar{u}, d,$  and  $\bar{d}$  quarks in the proton will be measured directly and precisely using maximal parity violation for production of  $W$  bosons in  $u\bar{d} \rightarrow W^+$  and  $d\bar{u} \rightarrow W^-$  [14, 15, 16, 17, 18].

Within the standard model,  $W$  bosons are produced through pure  $V-A$  interaction. Thus, the helicity of the participating quark and antiquark are fixed in the reaction. In addition, the  $W$  couples to a weak charge that correlates directly to flavors, if we concentrate on one generation. Indeed the production of  $W$ s in  $pp$  collisions is dominated by  $u, d, \bar{u},$  and  $\bar{d}$ , with some contamination from  $s, c, \bar{s},$  and  $\bar{c}$ , mostly through quark mixing. Therefore  $W$  production is an ideal tool to study the spin-flavor structure of the nucleon.

The leading-order production of  $W$  bosons,  $u\bar{d} \rightarrow W^+$ , is illustrated in Figure 1. The longitudinally polarized proton at the top of each diagram collides with an unpolarized proton, producing a  $W^+$ . At RHIC the polarized protons will be in bunches, alternately right- (+) and left- (-) handed. The parity-violating asymmetry is the difference of left-handed and right-handed production of  $W$ s, divided by the sum and normalized by the beam polarization:

$$A_L^W = \frac{1}{P} \times \frac{N_-(W) - N_+(W)}{N_-(W) + N_+(W)} . \quad (1)$$

We can construct this asymmetry from either polarized beam, and by summing over the helicity states of the other beam. The production of the left-handed weak bosons violates parity maximally. Therefore, if for example

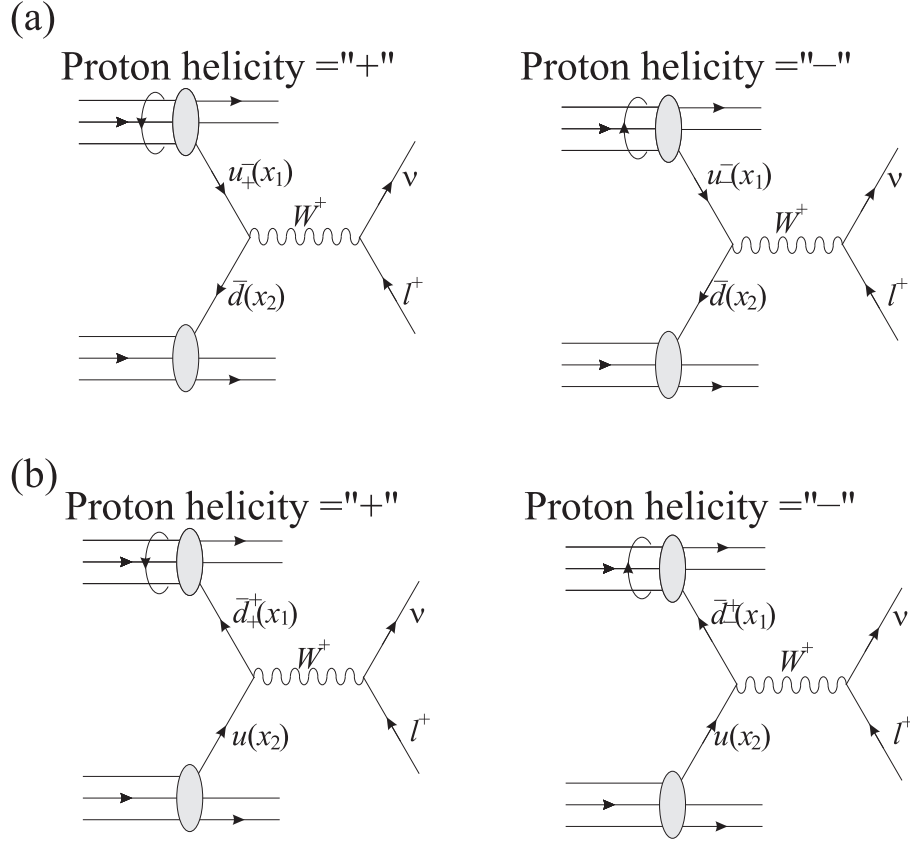


Figure 1: Production of a  $W^+$  in a  $\bar{p}p$  collision, at lowest order. (a)  $\Delta u$  is probed in the polarized proton. (b)  $\Delta \bar{d}$  is probed.

the production of the  $W^+$  proceeded only through the diagram in Figure 1a, the parity-violating asymmetry would directly equal the longitudinal polarization asymmetry of the  $u$  quark in the proton:

$$A_L^{W^+} = \frac{u_-(x_1)\bar{d}(x_2) - u_+(x_1)\bar{d}(x_2)}{u_-(x_1)\bar{d}(x_2) + u_+(x_1)\bar{d}(x_2)} = \frac{\Delta u(x_1)}{u(x_1)}. \quad (2)$$

Similarly, for Figure 1b alone,

$$A_L^{W^+} = \frac{\bar{d}_-(x_1)u(x_2) - \bar{d}_+(x_1)u(x_2)}{\bar{d}_-(x_1)u(x_2) + \bar{d}_+(x_1)u(x_2)} = -\frac{\Delta \bar{d}(x_1)}{\bar{d}(x_1)}. \quad (3)$$

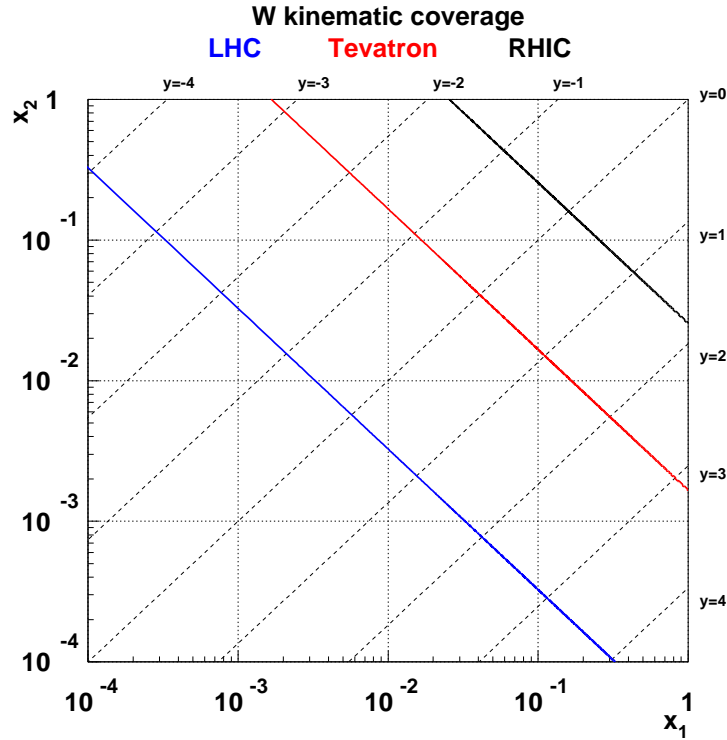


Figure 2:  $W$  kinematic coverage of  $x_1$  and  $x_2$  for different values of  $y$ ,  $-4 < y < 4$ , comparing RHIC at  $\sqrt{s} = 500$  GeV to the Tevatron kinematic region at  $\sqrt{s} = 1.96$  TeV and LHC at  $\sqrt{s} = 14$  TeV.

In general, the asymmetry is a superposition of the two cases:

$$A_L^{W^+} = \frac{\Delta u(x_1)\bar{d}(x_2) - \Delta\bar{d}(x_1)u(x_2)}{u(x_1)\bar{d}(x_2) + \bar{d}(x_1)u(x_2)}. \quad (4)$$

To obtain the asymmetry for  $W^-$ , one interchanges  $u$  and  $d$ .

For the  $pp$  collisions at RHIC with  $\sqrt{s} = 500$  GeV, the quark will be predominantly a valence quark. By identifying the rapidity of the  $W$ ,  $y_W$ , relative to the *polarized* proton, we can obtain direct measures of the quark and antiquark polarizations, separated by quark flavor:  $A_L^{W^+}$  approaches  $\Delta u/u$  in the limit of  $y_W \gg 0$ , whereas for  $y_W \ll 0$  the asymmetry becomes  $-\Delta\bar{d}/\bar{d}$ . Higher-order corrections change the asymmetries only a little [17, 18].

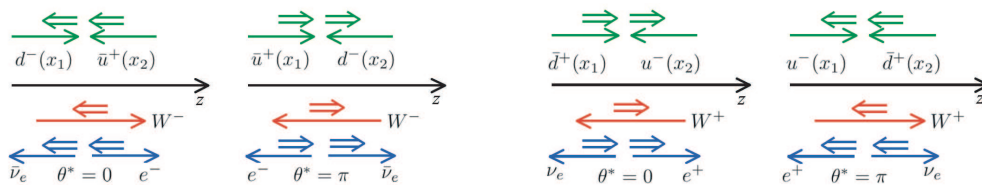


Figure 3: *Helicity configuration of  $W^-$  (left) and  $W^+$  (right) production showing on top the helicity configuration of the incoming quark and anti-quark. The middle panel shows the direction of the  $W$  spin. The lower panel displays the preferred direction of  $e^-/e^+$  quoting the scattering angle  $\theta^*$  in the  $W$  centre-of-mass system measured with respect to the positive  $z$  axis.*

The kinematics of  $W$  production and Drell-Yan production of lepton pairs is the same. The momentum fraction carried by the quarks and antiquarks,  $x_1$  and  $x_2$  (without yet assigning which is which), can be determined from  $y_W$ ,

$$x_1 = \frac{M_W}{\sqrt{s}} e^{y_W}, \quad x_2 = \frac{M_W}{\sqrt{s}} e^{-y_W}. \quad (5)$$

Note that this picture is valid for the predominant production of  $W$ s at  $p_T \sim 0$ . The experimental difficulty is that the  $W$  is observed through its leptonic decay  $W \rightarrow l\nu$ , and only the charged lepton is observed. We therefore need to relate the lepton kinematics to  $y_W$ , so that we can assign the probability that the polarized proton provided the quark or antiquark. Only then will we be able to translate the measured parity-violating asymmetry into a determination of the quark or antiquark polarization in the proton.

Figure 2 shows the  $W$  kinematic coverage of  $x_1$  and  $x_2$  for different values of  $y$ ,  $-4 < y < 4$ , comparing RHIC at  $\sqrt{s} = 500$  GeV to the Tevatron kinematic region at  $\sqrt{s} = 1.96$  TeV and LHC at  $\sqrt{s} = 14$  TeV. RHIC is in a unique position to constrain quark distribution functions, both unpolarized and polarized, at high Bjorken- $x$  where quark distribution functions exhibit larger uncertainties compared to lower values in Bjorken- $x$ .

The rapidity of the  $W$  is related to the lepton rapidity in the  $W$  rest frame ( $y_l^*$ ) and in the lab frame ( $y_l^{\text{lab}}$ ) by

$$y_l^{\text{lab}} = y_l^* + y_W, \quad \text{where } y_l^* = \frac{1}{2} \ln \left[ \frac{1 + \cos\theta^*}{1 - \cos\theta^*} \right]. \quad (6)$$

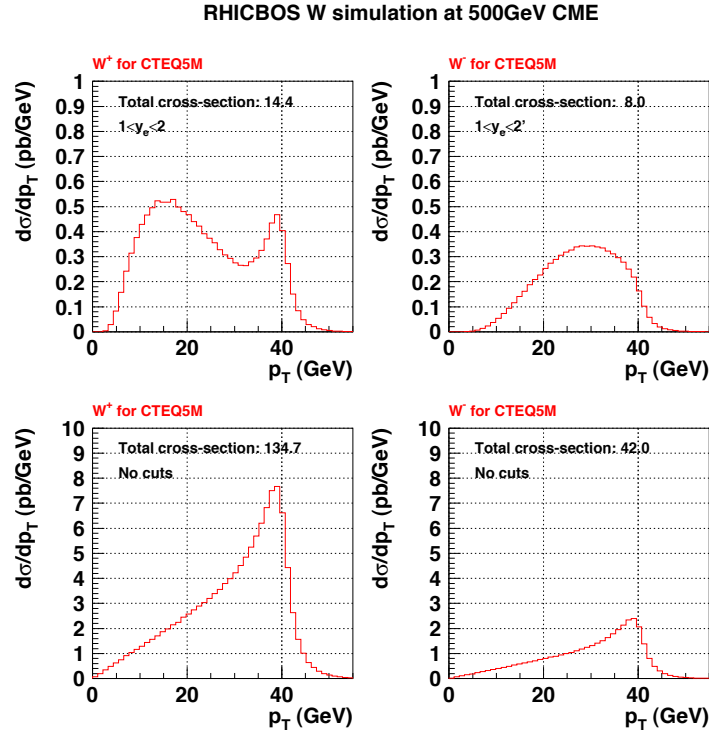


Figure 4: Leptonic  $p_T$  cross section for the  $W^+$  and  $W^-$  case with and without a cut on the electron rapidity of  $1 < y_e < 2$ .

Here  $\theta^*$  is the decay angle of the lepton in the  $W$  rest frame, and  $\cos\theta^*$  can be determined from the transverse momentum ( $p_T$ ) of the lepton with an irreducible uncertainty of the sign [19], since

$$p_T^{\text{lepton}} = p_T^* = \frac{M_W}{2} \sin\theta^*. \quad (7)$$

In this reconstruction, the  $p_T$  of the  $W$  is neglected. In reality, it has a  $p_T$ , resulting for example from higher-order contributions such as  $gu \rightarrow W^+d$  and  $ud \rightarrow W^+g$ , or from primordial  $p_T$  of the initial partons.

The Standard Model  $W$  boson is a purely left-handed current. The helicities of the respective quarks (negative helicity) and anti-quarks (positive helicity) are therefore fixed. The cross sections for  $W^+$  and  $W^-$  differential in  $y_W$  and the scattering angle  $\theta^*$  of the decay lepton in the  $W$  centre-of-mass system is given as follows:

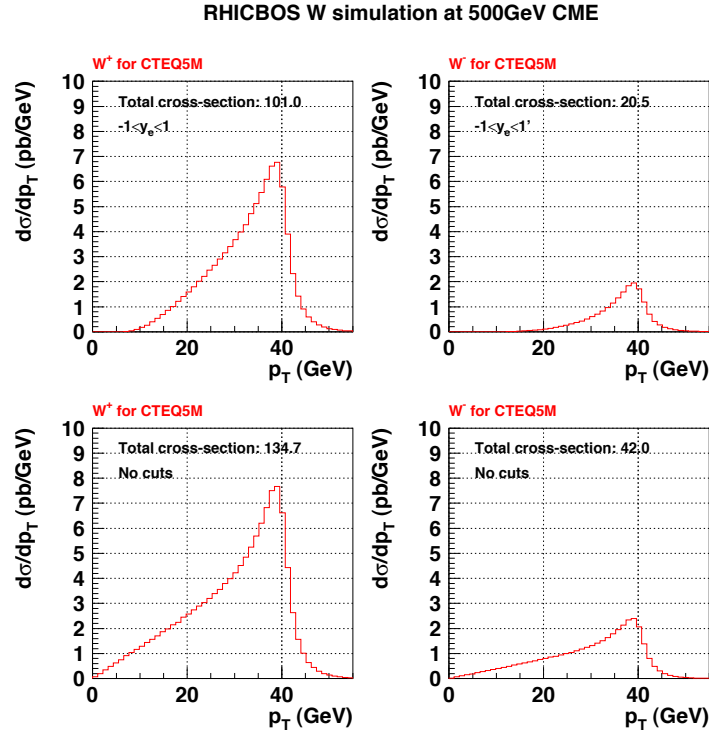


Figure 5: Leptonic  $p_T$  cross section for the  $W^+$  and  $W^-$  case with and without a cut on the electron rapidity of  $-1 < y_e < 1$ .

$$\left( \frac{d^2\sigma}{dy_W d \cos \theta^*} \right)_{W^+} \sim u(x_1)\bar{d}(x_2)(1 - \cos \theta^*)^2 + \bar{d}(x_1)u(x_2)(1 + \cos \theta^*)^2 \quad (8)$$

and

$$\left( \frac{d^2\sigma}{dy_W d \cos \theta^*} \right)_{W^-} \sim d(x_1)\bar{u}(x_2)(1 + \cos \theta^*)^2 + \bar{u}(x_1)d(x_2)(1 - \cos \theta^*)^2 \quad (9)$$

The characteristic dependence on the  $\theta^*$  is shown graphically in Figure 3 for the helicity configuration of  $W^-$  (left) and  $W^+$  (right) production. The top panel shows the helicity configuration of the incoming quark and anti-quark. The middle panel shows the direction of the  $W$  spin. The lower panel

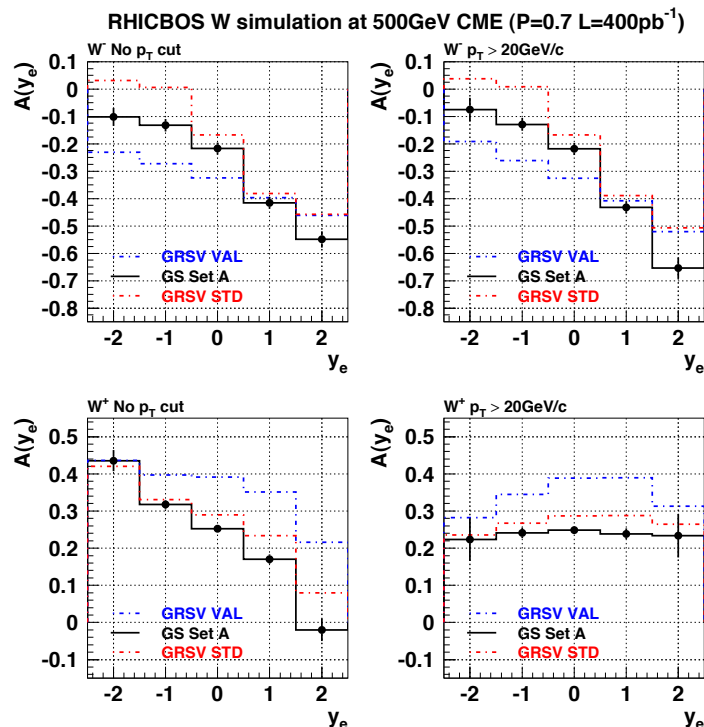


Figure 6: *The sensitivity to different underlying quark and anti-quark distributions based on GRSV-STD, GRSV-VAL [27] and GS-A [20]. GRSV-VAL considers a flavor asymmetry scenario of  $\Delta u$  and  $\Delta d$  whereas GRSV-STD is based on a flavor symmetry description.*

displays the preferred direction of  $e^-/e^+$  quoting the scattering angle  $\theta^*$  in the  $W$  centre-of-mass system measured with respect to the positive  $z$  axis.

Usually  $W$  production is identified by requiring charged leptons with large  $p_T$  and large missing transverse energy, due to the undetected neutrino. Since none of the detectors at RHIC is hermetic, measurement of missing  $p_T$  is not available, which leads to some background. Possible sources of leptons with high  $p_T$  include charm, bottom, and vector boson production. Above  $p_T \geq 20 \text{ GeV}/c$ , leptons from  $W$  decay dominate, with a smaller contribution from  $Z^0$  production. The additional background from misidentified hadrons is expected to be small at high  $p_T$ .

The sensitivity for STAR has been estimated using the RHICBOS MC

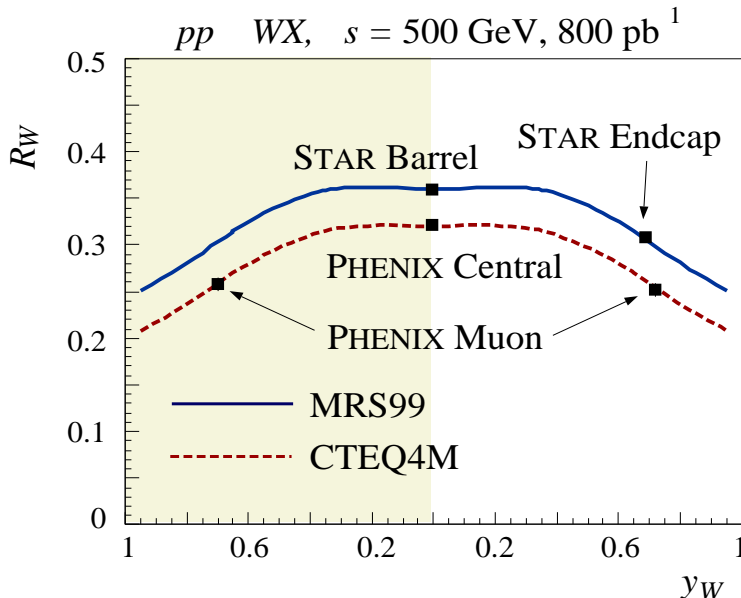


Figure 7: The ratio  $R_W = (d\sigma(W^-)/dy)/(d\sigma(W^+)/dy)$  for unpolarized  $pp$  collisions at RHIC. The shaded region indicates that unpolarized  $pp$  collisions are symmetric in  $y_W$ . To illustrate the sensitivity of the measurement, we show an earlier set of parton densities (CTEQ4M [25]) and a set (MRS99 [26]) that includes the latest information from Drell-Yan data [10]. Both curves include an asymmetric sea with  $\bar{d}/\bar{u}$  rising to 1.6 for increasing antiquark momentum fraction  $x_{\bar{q}}$ , but the latter also includes a drop-off in the ratio for higher  $x_{\bar{q}}$ .

program [2] based on a calculation for resummation of large logarithmic contributions originating from multiple soft gluon contribution. This framework allows the prediction of the leptonic longitudinal single-spin asymmetry for various distribution functions taking into account the impact of leptonic cuts such as  $p_T$ . The STAR Electromagnetic Endcap Calorimeter (EEMC) spans the region of  $1 < y_e < 2$ .

Figure 4 (5) shows the leptonic  $p_T$  cross section for the  $W^+$  and  $W^-$  case with and without a cut on the electron rapidity of  $1 < y_e < 2$  ( $-1 < y_e < 1$ ). The sensitivity to different distribution functions of the underlying quark and anti-quark distributions based on GRSV-STD, GRSV-VAL [27] and GS-A [20] is shown in Figure 6. GRSV-VAL considers a flavor asymmetry scenario of  $\Delta u$  and  $\Delta d$  whereas GRSV-STD is based on a flavor symmetry description.

The projections in Figure 6 are shown for a beam polarization of 70% and an integrated luminosity of  $400 \text{ pb}^{-1}$ . Clear discrimination power to the choice of the underlying distribution function is seen in the forward direction in case of  $W^-$  production. For  $W^+$  production, the sensitivity is similar in the forward and barrel region.

RHIC will also significantly contribute to our knowledge about the unpolarized parton densities of the proton, since it will have the highest-energy  $pp$  collisions.  $\bar{p}p$  production of  $W$ s has a much stronger valence component in the determined [23]  $u(x)/d(x)$  ratio. Isospin dependence in Drell-Yan production of muon pairs in  $pp, pd$  scattering [10], violation of the Gottfried sum rule [24, 9], and recent semi-inclusive DIS measurements [11] have shown that the unpolarized sea is not  $SU(2)$  symmetric. At RHIC, the ratio of unpolarized  $W^+$  and  $W^-$  cross sections will directly probe the  $\bar{d}/\bar{u}$  ratio, as shown in Figure 2.3.

Forward scattered tagged in the STAR EEMC ( $1 < \eta < 2$ ) off the incoming polarized proton beam moving toward (away) from the STAR EEMC, yield a purity for coming from quarks of about 98% (75%). The separation of from hadronic background will be important and therefore the full exploitation of the STAR EEMC with its intrinsic means for e/h separation (pre-shower and post-shower readout system) will be crucial. The discrimination of quark combinations requires distinguishing between high  $p_T$  charged leptons through their opposite charge sign which in turn requires precise tracking information. The resolution of the STAR Time-Projection Chamber (TPC) deteriorates rapidly beyond  $|\eta| > 1$ . It does not permit charge discrimination for high  $p_T$  tracks.

## 3 Layout and simulation results

### 3.1 Overview

The proposed STAR Forward GEM Tracker (FGT) is part of an integrated tracking upgrade for the STAR experiment. The upgrade of the inner tracking system for  $-1 < \eta < +1$  is configured as barrels around the interaction point and consist of two layers of the Heavy Flavor Tracker (HFT), 2 layers of the Intermediate Silicon Tracker (IST) and one layer of the existing Silicon Strip Detector (SSD). The HFT will act as a  $\mu$ -vertex detector and is described in a separate document [28]. The SSD has already been installed in STAR and will not be discussed here. The IST is described separately [29].

The forward tracking detectors cover  $+1 < \eta < +2$ . The six triple-GEM type disks of the Forward GEM Tracker (FGT) can be seen in Figure 8. Tracks of electrons with  $E_T$  of 40 GeV are overlayed for three different  $\eta$  values (1.0, 1.5, 2.0), originating from three  $Z$  vertex locations at  $-30$  cm,  $0$  cm and  $+30$  cm. Also visible is the multi-layer barrel inner tracking system based on the HFT, IST and SSD. In addition a previous FST+FGT configuration is shown. It consists of four FGT disks and four silicon disks (FST) at smaller radii closer to the interaction region.

Several options have been studied based on disk and barrel arrangements. The proposed configuration based on six triple-GEM disk detectors and no FST disks addresses several issues such as optimized acceptance taking into account the  $Z$  vertex distribution with a Gaussian sigma of about 30 cm. The proposed inner fast tracking system (IST and SSD) will be essential to provide precise hit information supplementing TPC hits to constrain high- $p_T$  tracks for  $Z < 0$ . This underlines the importance of those inner tracking elements also for the future  $W$  physics program. The proposed configuration provides a cost effective solution based only on GEM technology. The usage of additional silicon disks (FST) at smaller radii as originally anticipated does not yield an improvement in performance and is no longer considered. GEM technology is widely employed by current and future experiments in nuclear and particle physics. A SBIR proposal (Phase 1 and Phase 2) has been approved and is the basis for the industrial production of GEM foils to be used for the forward GEM tracking system. The readout system for both the intermediate (IST) and forward (FGT) tracking systems are based on the APV25-S1 readout chip which has been extensively tested for the CMS sili-

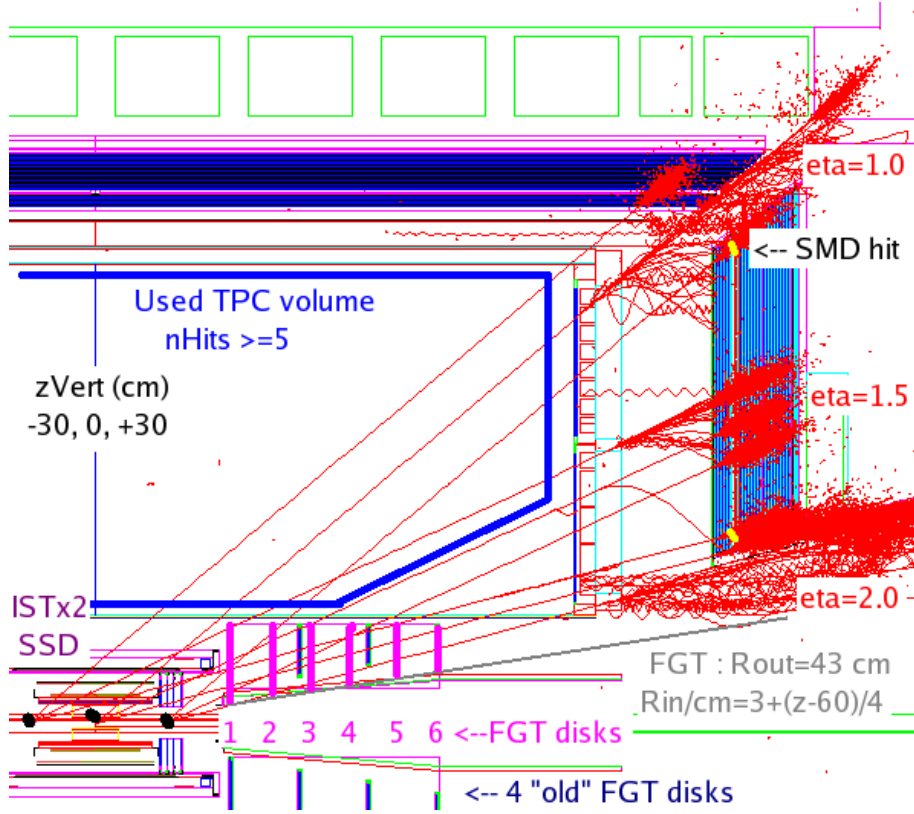


Figure 8: *Layout of the Forward GEM Tracker, consisting of six triple-GEM detector disks. Tracks of electrons with 40 GeV ET are overlaid from three Z vertex locations at  $-30$  cm,  $0$  cm and  $+30$  cm with three different  $\eta$  values of 1.0, 1.5 and 2.0 for each vertex location. Also visible is the multi-layer barrel inner tracking system based on the HFT, IST and SSD. The previous FGT configuration is shown at the bottom. Former FST is not used in current layout.*

con tracker and is also used by the COMPASS triple-GEM tracking stations. A common chip readout system will significantly simplify the design of the overall readout system for the integrated tracking upgrade. The proposed configuration is based on light-weight materials to limit the amount of dead material in the forward direction. It also provides the possibility to decouple the inner and forward tracking system from a mechanical perspective. In summary, the charge-sign discrimination of high- $p_T$   $e^{-(+)}$  to distinguish

$W^{-(+)}$  bosons is based on using a beam line constraint, precise hit information from six triple-GEM disks, IST+SSD, hits at forward  $\eta$  from the TPC and the electromagnetic-cluster hit information from the shower-maximum detector of the STAR EEMC.

The requirements for a forward tracking system for the future STAR W physics program will be summarized in the next section followed by a discussion of simulations on electron/hadron separation and high- $p_T$   $e^{-(+)}$  charge sign discrimination.

## 3.2 Requirements

**General** The FGT serves the  $W$ -physics spin program at 500 GeV center-of-mass energy in p+p collisions. Optimization for operation in a high-multiplicity environment as required for a relativistic-heavy ion program has not been considered to be a stringent requirement in the design.

**Geometric constraints** The forward STAR tracker configuration is designed to fit within the STAR detector configuration. The design has to limit the amount of additional dead material in the forward direction.

**Charge discrimination** The FGT should extend charge discrimination with the existing STAR Time Projection Chamber (TPC) for highly energetic  $e^-/e^+$  from  $W^-$  and  $W^+$  boson decays in the pseudo-rapidity region of  $1 < \eta < 2$  that is covered by the existing STAR EEMC. Figure 9 shows a comparison of RHICBOS and PYTHIA simulation results for the  $p_T$  spectra of  $e^-/e^+$  with no  $\eta$  cut, a cut on the forward acceptance of  $1 < \eta < 2$  and a cut at mid-rapidity of  $-1 < \eta < 1$ . The lower  $p_T$  region is more enhanced for forward rapidities in comparison to the mid-rapidity region. Figure 10 shows the value of sagitta in mm as a function of  $p_T$  and  $\eta$  for the forward upgrade configuration with the first hit at the event vertex and the last at the location of the STAR EEMC shower-maximum detector. The correlation is shown for a sample of events generated flat in  $p_T$  ( $5 < p_T < 40$  GeV/c) and  $\eta$  ( $1 < \eta < 2$ ). The forward tracking system in combination with existing STAR detector components has to be able to provide charge sign discrimination with high efficiency for  $e^-/e^+$  for sagitta values as low as 0.5 mm at the highest  $p_T$  (40 GeV/c) and  $\eta$  (2) values.

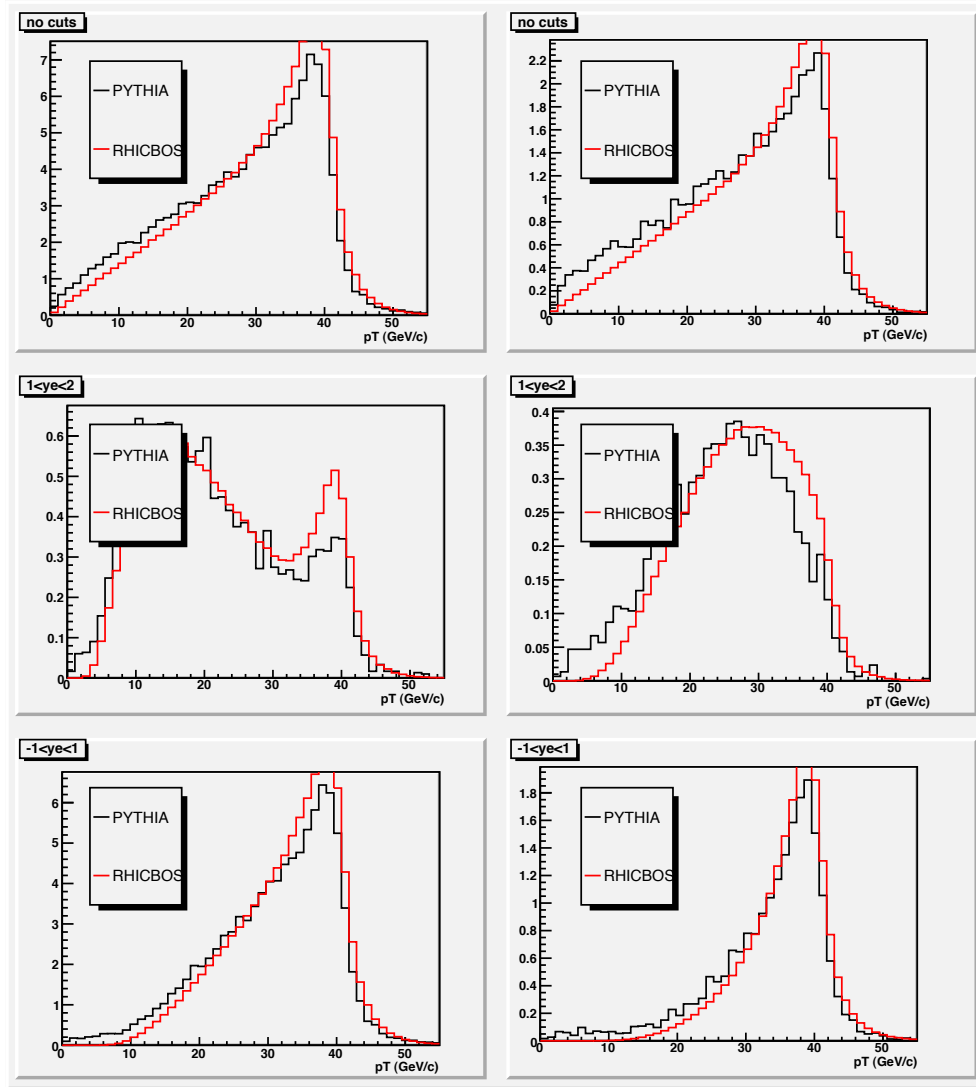


Figure 9: Comparison of RHICBOS and PYTHIA simulation results for the  $p_T$  spectra of  $e^-$  (left column) and  $e^+$  (right column) with no  $\eta$  cut, a cut on the forward acceptance of  $1 < \eta < 2$  and a cut at mid-rapidity of  $-1 < \eta < 1$ . The lower  $p_T$  region is more enhanced for forward rapidities in comparison to the mid-rapidity region.

**e/h separation** The suppression of hadronic background will be essential. This will be based on the usage of various EEMC readout elements (Pre- and

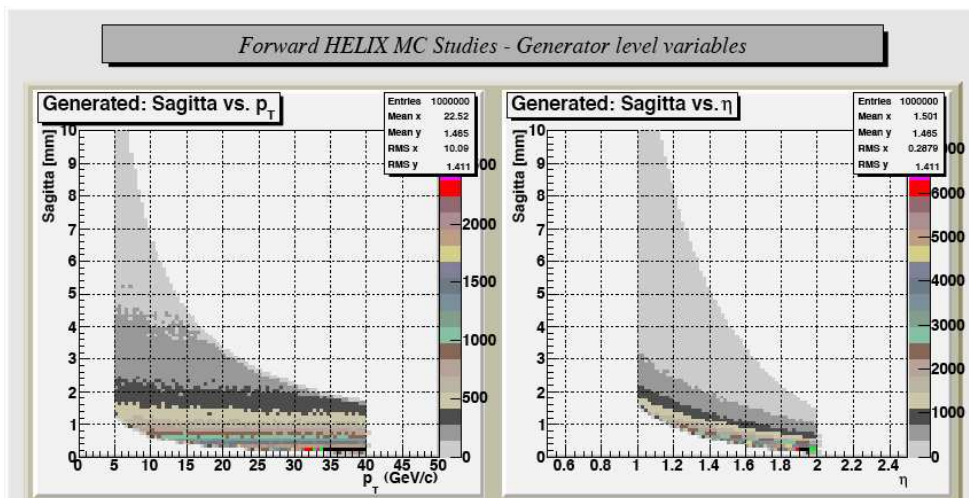


Figure 10: *Sagitta* in mm as a function of  $p_T$  and  $\eta$  for the forward upgrade configuration with the first hit at the event vertex and the last at the location of the STAR EEMC shower-maximum detector. The correlation is shown for a sample of events generated flat in  $p_T$  ( $5 < p_T < 40$  GeV/c) and  $\eta$  ( $1 < \eta < 2$ ).

post-shower layers, total energy and shower-maximum detector) to provide an effective means for e/h separation through transverse and longitudinal shower shape discrimination.

**Intrinsic sampling speed** The spin program at RHIC requires the discrimination of individual beam bunches having a bunch crossing time of 107 ns. The FGT should be able to resolve individual beam bunches.

**Rate capability** The FGT should be able to handle the full RHIC-II peak luminosity of  $4 \cdot 10^{32} \text{cm}^{-2} \text{s}^{-1}$  at a center-of-mass energy of 500 GeV in p+p collisions.

**Pileup suppression** At the RHIC-II peak luminosity, one expects on average 1.7 minbias collisions per trigger per bunch crossing. The piled up tracks from charged  $\pi^+$ ,  $\pi^-$  should be rejected using e/h discrimination and total energy available from the STAR EEMC. One expects 10-20 such tracks at  $\eta \in [1, 2]$ . This will be addressed with further MC simulations.

**Readout system** A common chip readout system of the IST and FGT will significantly simplify the design of the overall readout system for the integrated tracking upgrade.

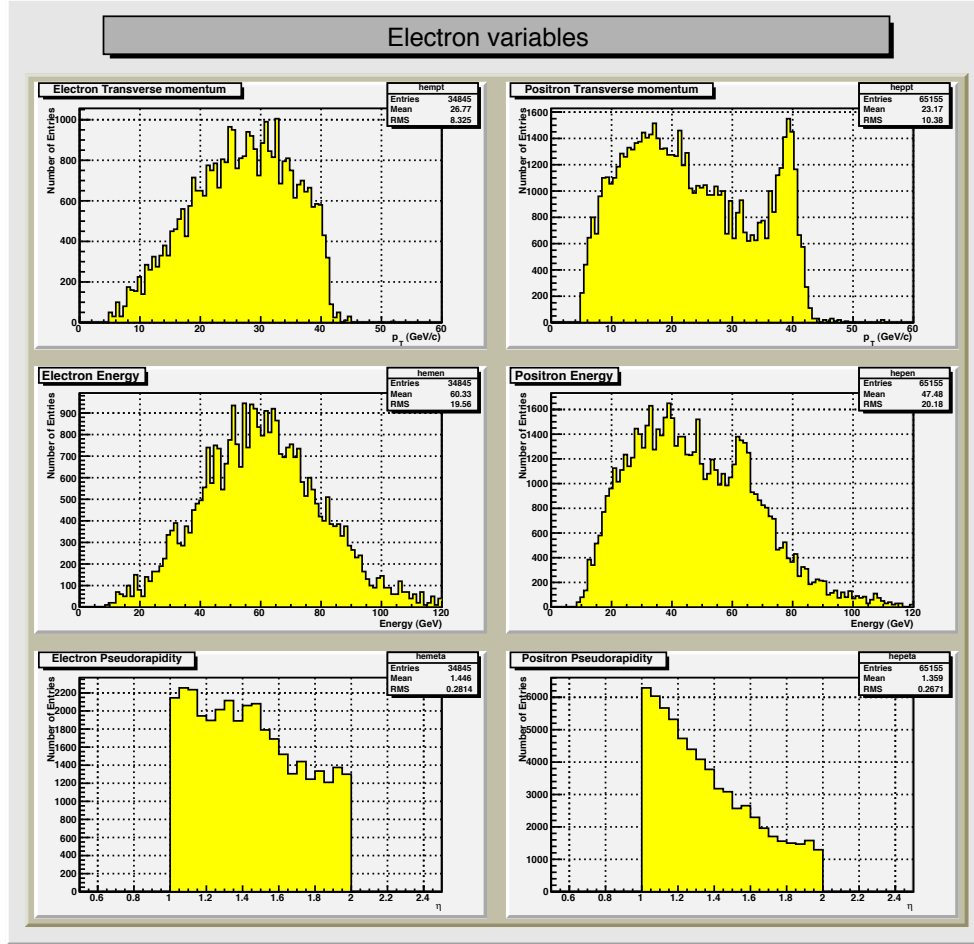


Figure 11: *Transverse momentum and total energy of electrons/positrons in  $W$  production in the STAR EEMC acceptance region. A measurement of  $E_T$  in the STAR EEMC with an accuracy of a few percent will be possible.*

**Trigger** The basic trigger requirement for high- $p_T$  electrons/positrons will be based on a high-tower (HT) trigger of the STAR EEMC. The STAR EEMC will allow a precise measurement of  $E_T$ . Figure 11 shows the total

energy of electrons/positrons in  $W$  production in the STAR EEMC acceptance region. A measurement of  $E_T$  in the STAR EEMC with an accuracy of a few percent will be possible.

### 3.3 Simulation results

Detailed simulations have been performed on the question of e/h separation and  $e^-/e^+$  charge-sign discrimination, which will be described in the following two sections along with an overview of the simulation tools.

**e/h separation** The STAR EEMC provides a powerful set of individual calorimeter elements for efficient e/h discrimination through transverse and longitudinal shower shape discrimination. Those are based on the STAR EEMC pre-shower layers, the shower maximum detector, the individual calorimeter towers and the post-shower layer. Electromagnetic showers are expected to be narrower and develop earlier compared to hadronic showers. Figure 12 shows the ratio of the energy of various STAR EEMC calorimeter elements to the total energy. The ratios are shown from top to bottom for both pre-shower energies separately, the shower-maximum U and V energies, the tower energy and the post shower energy. The red line refers to the case of a single 10 GeV pion whereas the black line refers to the response of a 10 GeV electron. The difference in the shower development from pions compared to electrons is clearly visible in these distributions.

Figure 13 shows the  $p_T$  distributions for charged hadrons from a PYTHIA MC sample in comparison to a PYTHIA MC sample of electrons from  $W$  events. A drastic reduction in background can be achieved while retaining most of the  $W$  signal events by requiring isolation cuts and a missing  $p_T$  cut, and at 40 GeV these already appear sufficient. These two criteria together with an  $E/p$  cut should allow a reduction of hadronic background over signal at a level of  $10^3$ . Additional gains are expected from cuts on energy deposition vs. depth in the calorimeter based on quantities shown in Figure 12, and will be needed to preserve suitable signal to background ratios at lower  $p_T$  where increasing hadronic background can dominate the electron/positron signal we seek. Triggering on the high energy electromagnetic signals at high efficiency will be possible at acceptable rates by using a threshold on energy deposition in the calorimeter. We note that such a trigger already suppresses hadronic background.

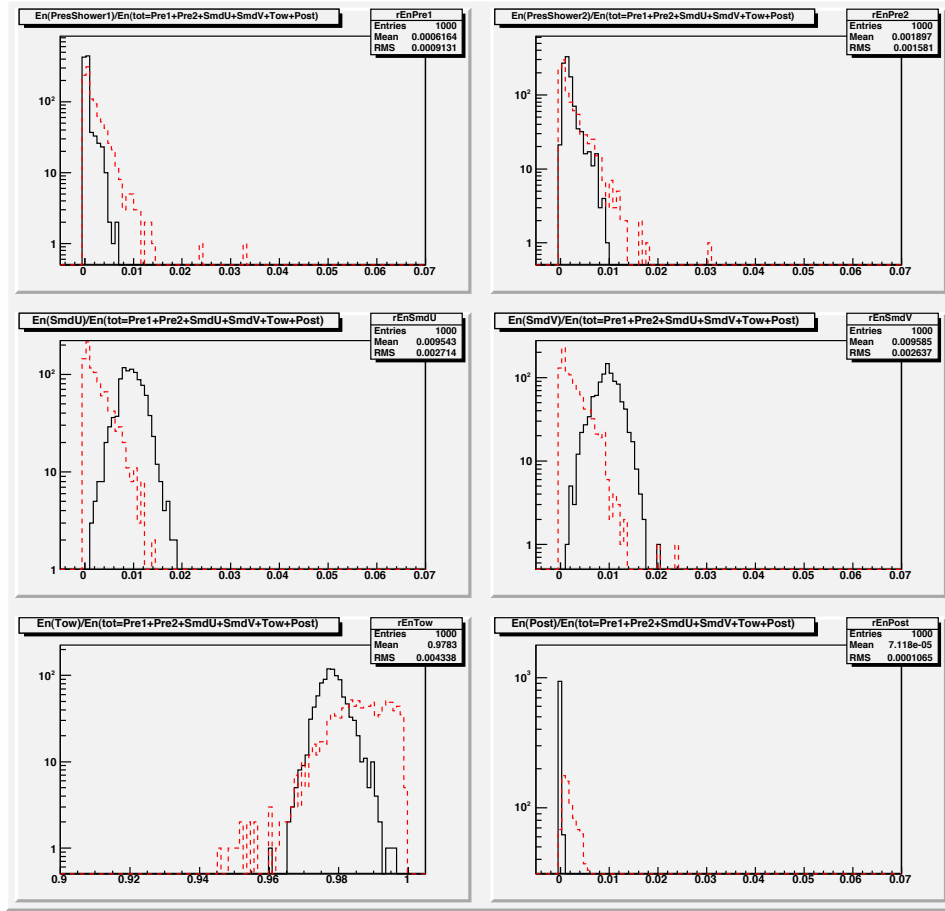


Figure 12: *Ratio of the energy of various STAR EEMC calorimeter elements to the total energy. The ratios are shown from top to bottom for both pre-shower energies separately, the shower-maximum U and V energies, the tower energy and the post shower energy. The red line refers to the case of a single 10 GeV pion whereas the black line refers to the response of a 10 GeV electron. The difference in the shower development form pions compared to electrons is clearly visible in these distributions.*

**$e^-/e^+$  separation** Two independent paths have been chosen to optimize the forward tracking configuration. One, which models the location of various tracking elements and their Gaussian errors will be referred to as HELIX MC model ignoring the impact of dead material. This approach has been

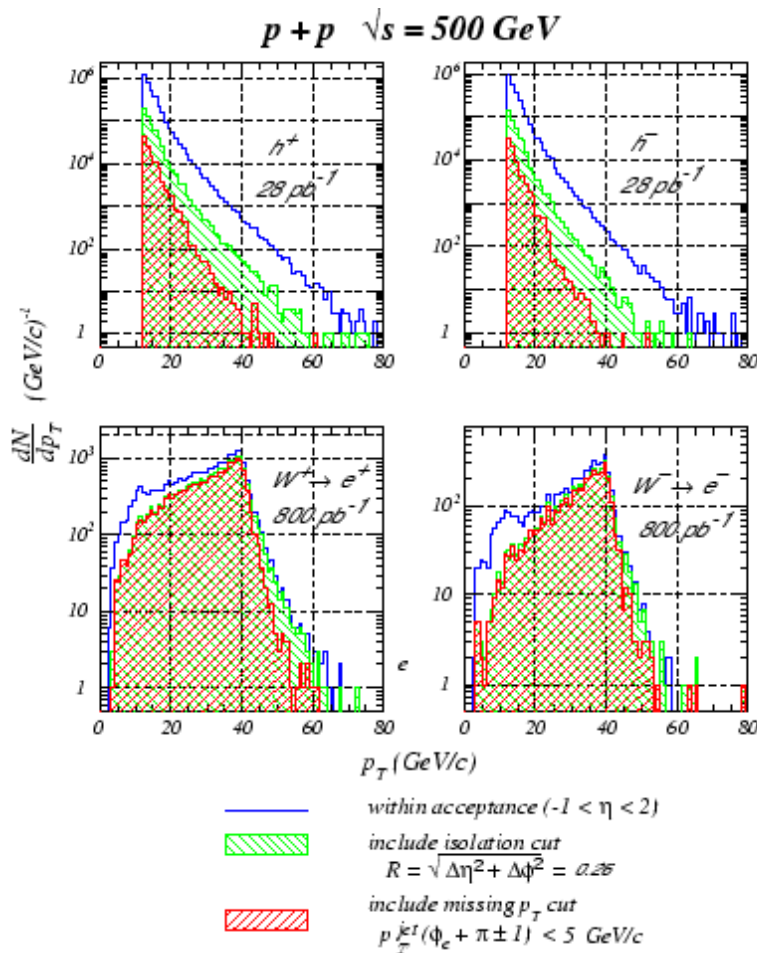


Figure 13:  $p_T$  distribution for charged hadrons from a PYTHIA MC sample including detector effects in comparison to a PYTHIA MC sample of electrons from  $W$  events. A drastic reduction in background can be achieved while retaining most of the  $W$  signal events by requiring an isolation criteria and a missing  $p_T$  cut. These two criteria together with an  $E/p$  cut will allow a reduction of background over signal at level of  $10^3$ .

chosen to provide a quick turn-around of acceptance studies for varying detector configurations. At high  $p_T$  as is the case for the  $W$  program, multiple scattering is expected to play a minimal role. The second simulation chain is fully based on the STAR reconstruction framework starting from the STAR

GEANT model (STARSIM) followed by the STAR reconstruction chain.

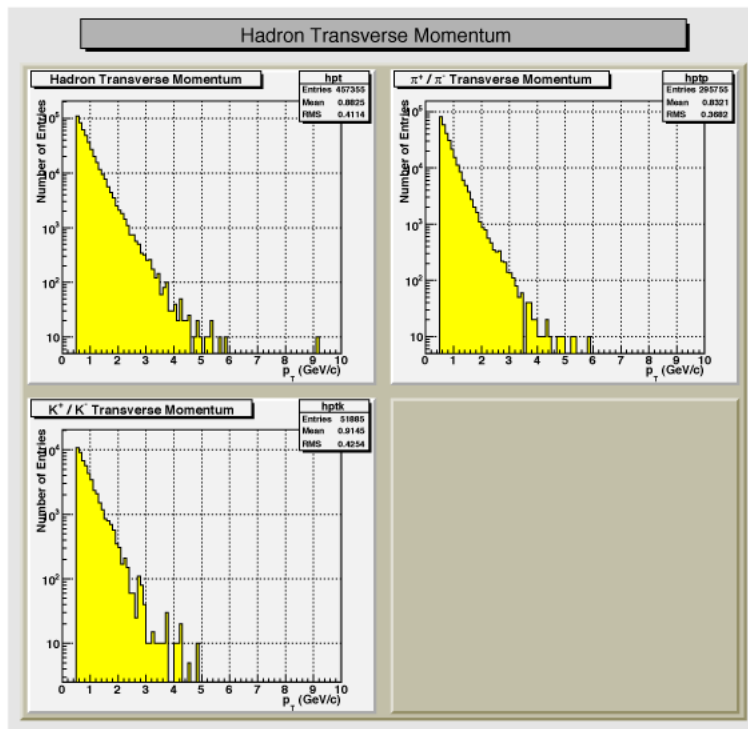


Figure 14: *PYTHIA* prediction of hadron  $p_T$  for  $\sqrt{s} = 500$  GeV  $W$  production in  $p+p$  collisions.

Let us first consider the various hits used to constrain a high- $p_T$  track. One expects that  $W$ -events will contain very few primary tracks at mid rapidity. Figures 14 and 15 shows the  $p_T$  and multiplicity distribution of pions and kaons from a *PYTHIA*  $W$  event simulation. Often only the electron/positron from  $W$  decay will be detectable for  $-1 < \eta < 2$ . Hence it is very likely one will not be able to reconstruct the primary vertex position on an event-by-event basis before the electron track itself is found. The following simulation result will not assume a reconstructed event vertex on an event-by-event basis. However, a beam-line constraint is taken into account. Both colliding beams are well focused with a transverse profile of the interaction diamond in both transverse directions of about  $250 \mu\text{m}$  at 200 GeV center-of-mass energy. It is expected that the transverse beam size is further reduced by a factor  $\sqrt{2.5}$  in case of 500 GeV center-of-mass energy. The transverse position of the

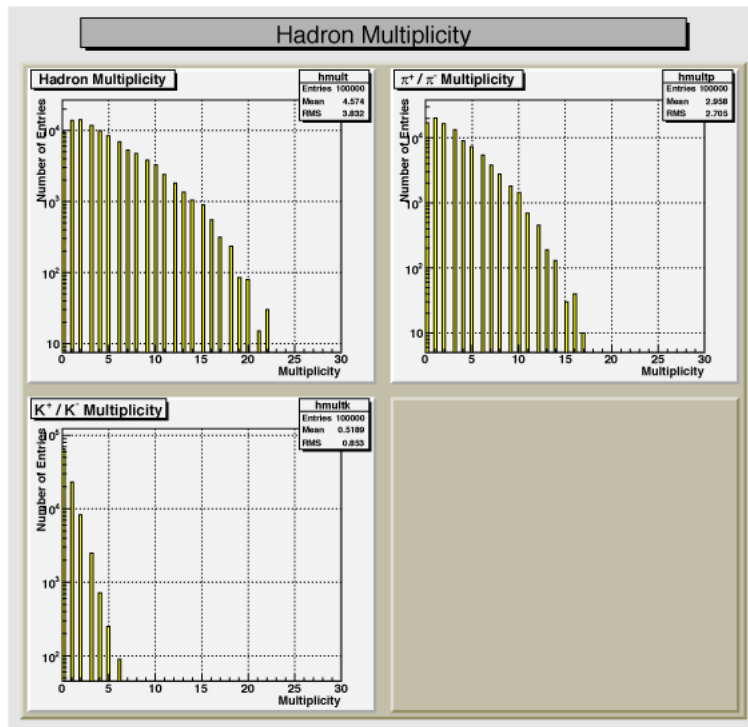


Figure 15: *PYTHIA* prediction of hadron multiplicity spectra for  $\sqrt{s} = 500$  GeV  $W$  production in  $p+p$  collisions. A cut of  $p_T > 0.5$  GeV/ $c$  and  $-2 < \eta < 2$  has been imposed on every final state hadron.

interaction diamond is rather stable and changes typically by approximately  $100 \mu\text{m}$  [31]. The beam line constraint is routinely determined and used at STAR for various TPC related analyses.

In the Helix reconstruction it is assumed that the transverse vertex position is known with a Gaussian sigma of  $200 \mu\text{m}$ . The impact of a larger transverse beam size has been evaluated as minor effect and will be discussed below. The  $Z$  vertex location of thrown electrons has been initially fixed at  $-30$  cm,  $0$  cm and  $+30$  cm and subsequently smeared in reco with a Gaussian sigma of  $30$  cm. This choice was made to ensure that the proposed forward tracking system provides good acceptance and proper charge sign discrimination over a large  $Z$  vertex region. This is essential considering the small cross-section for  $W$  production at  $\sqrt{s} = 500$ . In the Helix reconstruction the following detectors are used: IST1, IST2, SSD, six FGT disks, TPC and

Detector	Resolution	Remarks
Vertex	200 $\mu\text{m}$ in $X, Y$	Added as hit
IST1	20 $\mu\text{m}$ in $r\phi$	
IST2	500 $\mu\text{m}$ in $r\phi$	
SSD	20 $\mu\text{m}$ in $r\phi$	
FST *)	20/60 $\mu\text{m}$ in $X, Y$	2 disks (1+4)
FGT	60 $\mu\text{m}$ in $X, Y$	6 disks
EEMC SMD	1.5 mm in $X, Y$	

Table 1: *Helix hit parameters. (The FST is used only in some configurations to justify its removal).*

ESMD and a vertex hit based on a beam line constraint. The hit points predicted by GEANT are smeared with Gaussian distributions as described in Table 1 and weights are assigned accordingly. It has been shown that the STAR EEMC shower-maximum detector provides a hit resolution at the level of 1.5 mm (Figure 16). If less than 5 hits are found in working TPC padrows (2-12, 14-45) all TPC hits are discarded and the tracker will use only fast detector points + vertex. The reason is that pileup in the TPC may prevent a reliable reconstruction of short track segments. The 5-point seed is a nominal value used in the current TPC reconstruction software. If less than 5 hits (including vertex) are available from any detectors the track is declared to be not valid. The helix fit consists of two consecutive steps. First 2D circle parameters are calculated based on  $(x, y, weight)$  values using a standard circle-fit algorithm. The resulting 3 output parameters are  $X_0$ ,  $Y_0$  of the center of the circle and its radius  $R$ . Next the straight line 2D fit is performed in the  $R_{xy} - Z$  plane using  $(X_0, Y_0)$  from the circle fit. The reconstructed track is declared as valid if the deviation between the original (thrown) and reconstructed momentum direction at the primary vertex deviates less than 3 mrad in theta and phi directions. This cut translates to a displacement of about 1 cm of projected track at the ESMD plane. The charge of the reconstructed track is determined based on the sign of the curvature of the circle fit. It has been checked that the  $\chi^2/ndf$  from the circle fit is approximately 1.

Figures 17, 18, and 19 show the correlation of the radius of hits in the detectors,  $R_{xy}$  as a function of  $\eta$  for a fixed  $Z$  vertex location at 0 cm,  $-30$  cm, and  $+30$  cm. The TPC hits are shown as blue hits separating the inner and outer pad rows. The gap in-between refers to pad row 13 which has been

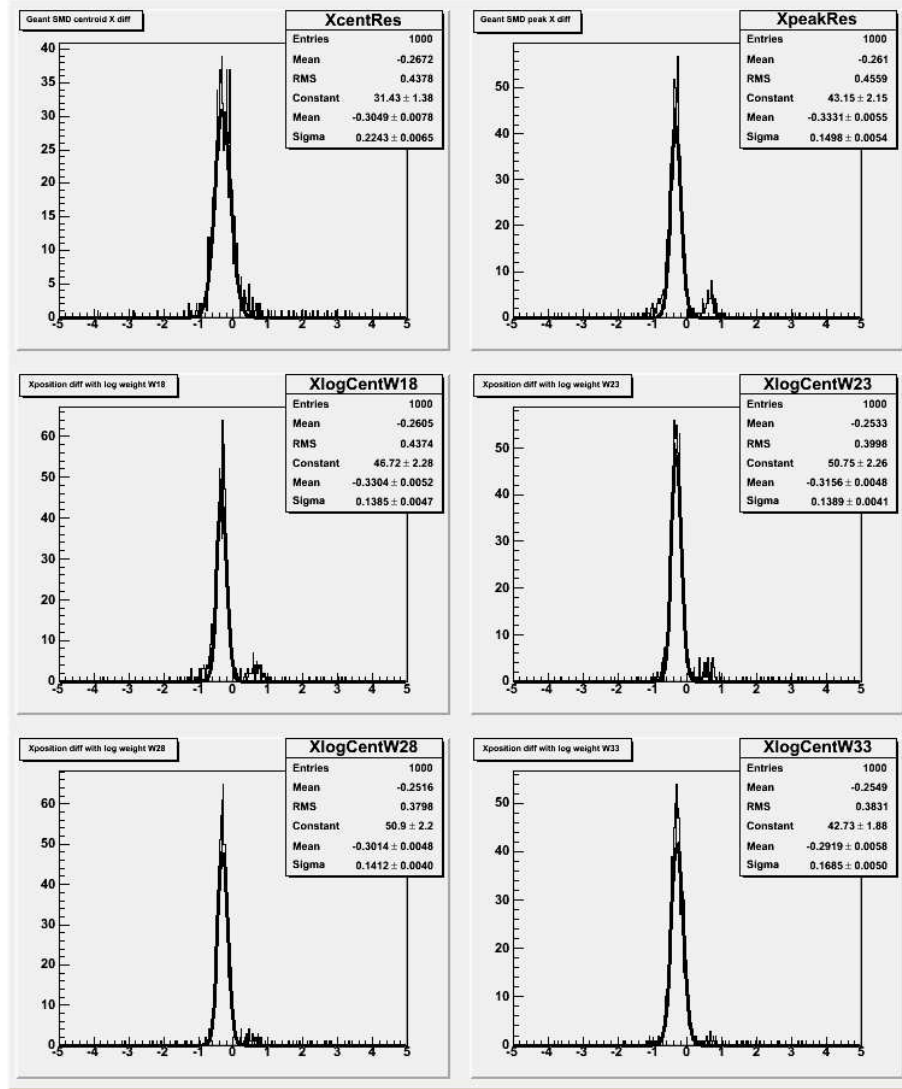


Figure 16: Position resolution for log-weighting method of STAR EEMC shower-maximum strip information [30] for different shower tail cut-off parameters are shown in the lower 4 panels. The upper two panels show position resolutions for 2 methods using linear weighting.

excluded. The red hits refer to the STAR EEMC shower-maximum detector hit. For  $Z = -30$  cm (Figure 18), the SSD and IST1/2 cover almost the full  $\eta$  range for  $1 < \eta < 2$ . The hit location of the FGT is shown in magenta,

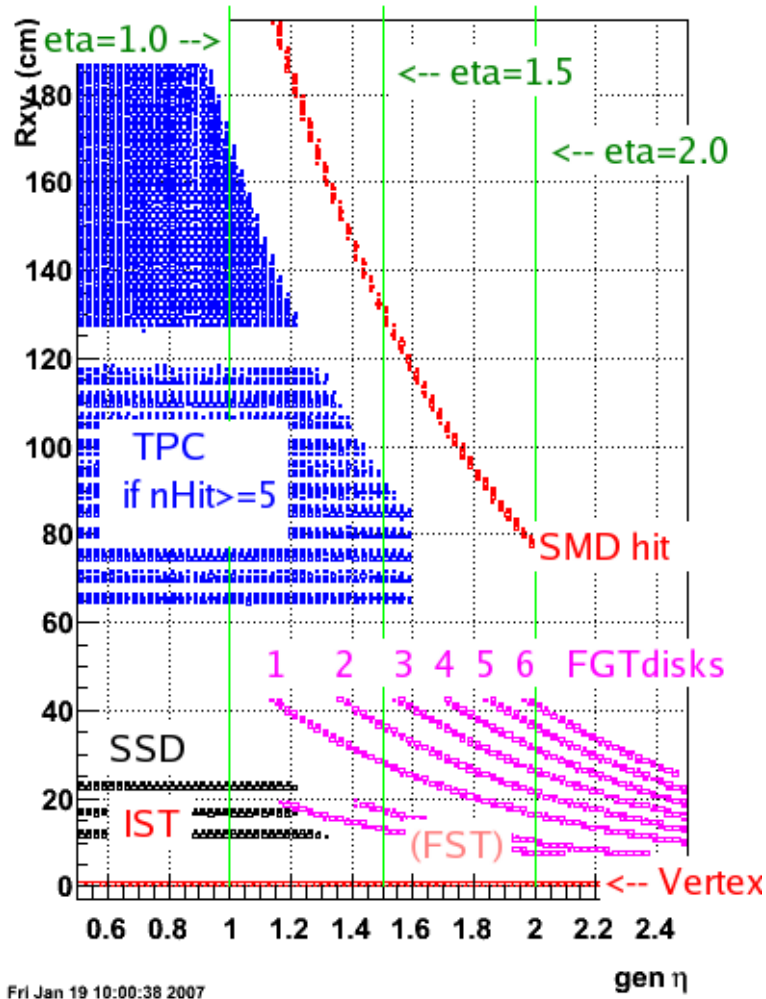


Figure 17: Correlation of  $R_{xy}$ , the radius of hits in the detectors, as a function of  $\eta$  for a fixed  $Z$  vertex location at 0 cm. The TPC hits are shown as blue hits separating the inner and outer pad rows. The gap in between is pad row 13 which has been excluded. The red hits are the STAR EEMC shower-maximum detector hits. The hit location of the FGT is shown in magenta.

which covers in particular the region for  $\eta > 1.5$ . The FGT becomes more important at  $Z = 0$  and is essential for  $Z = +30\text{cm}$ . The initial inner silicon disk arrangement (FST) has only some minor impact around the nominal interaction region at  $Z = 0\text{cm}$ .

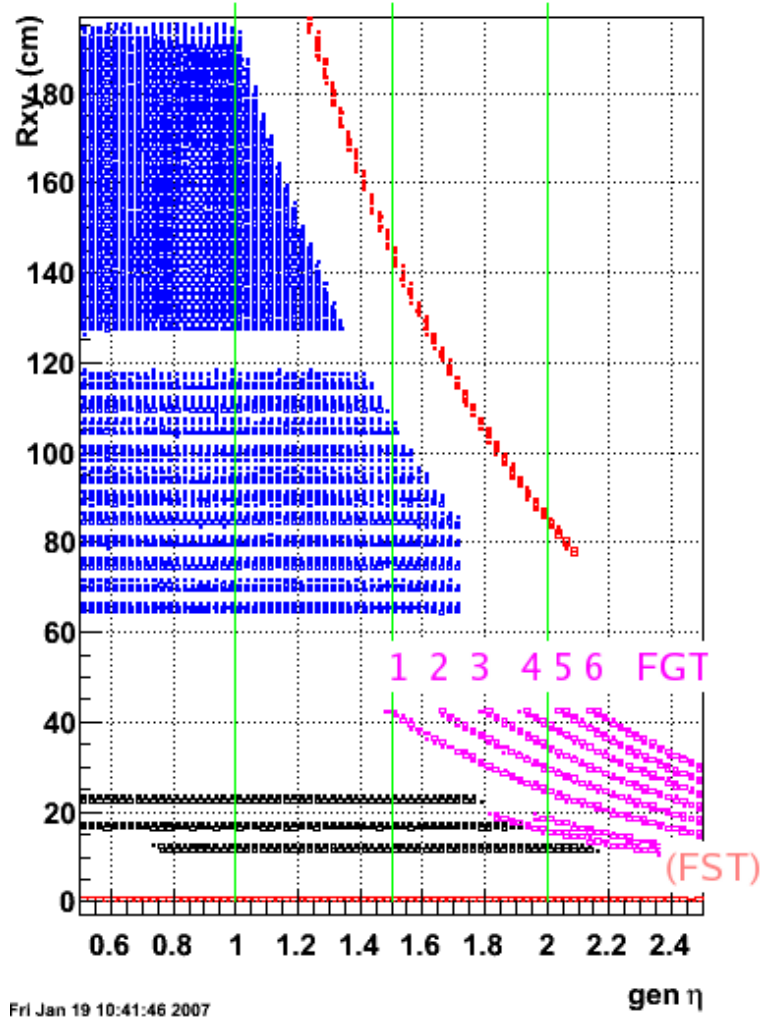


Figure 18: Correlation of  $R_{xy}$ , the radius of hits in the detectors, as a function of  $\eta$  for a fixed  $Z$  vertex location at  $-30$  cm. The TPC hits are shown as blue hits separating the inner and outer pad rows. The gap in between is pad row 13 which has been excluded. The red hits are the STAR EEMC shower-maximum detector hits. The hit location of the FGT is shown in magenta. This is the same as Figure 17, except for the vertex position.

All simulation results on the track reconstruction efficiency and charge sign discrimination probability will be shown (Figure 20-23) for three  $Z$  ver-

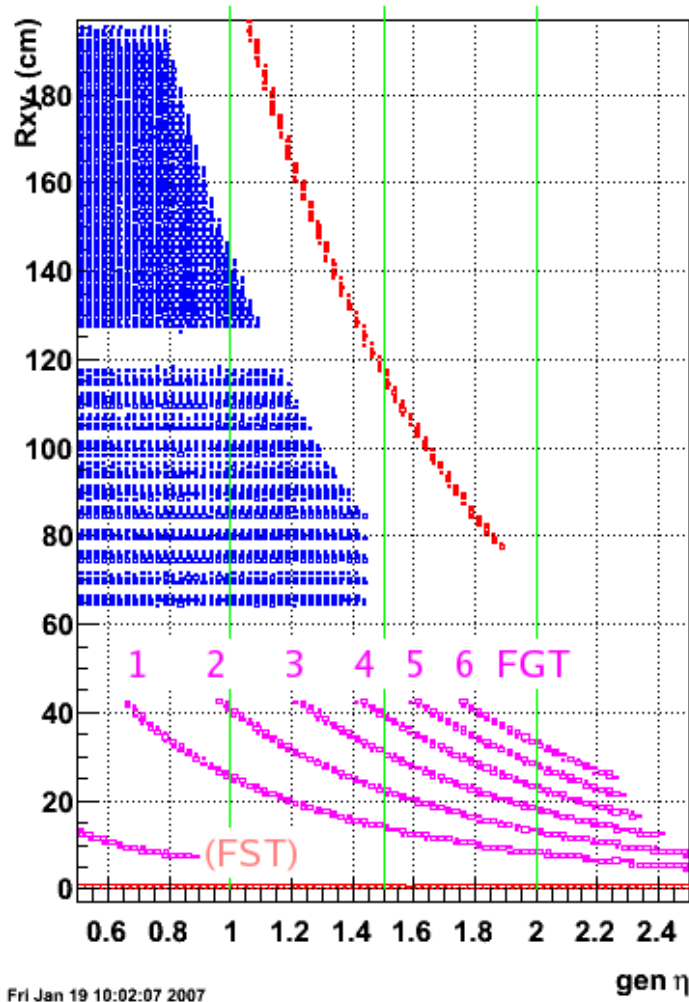


Figure 19: Correlation of  $R_{xy}$ , the radius of hits in the detectors, as a function of  $\eta$  for a fixed  $Z$  vertex location at  $+30$  cm. The TPC hits are shown as blue hits separating the inner and outer pad rows. The gap in between is pad row 13 which has been excluded. The red hits are the STAR EEMC shower-maximum detector hits. The hit location of the FGT is shown in magenta. This is the same as Figure 17, except for the vertex position.

text locations at  $-30$  cm,  $0$  cm and  $+30$  cm. Single tracks generated flat in  $\eta$  and  $\phi$  with  $p_T = 30$  GeV/c have been used. All configurations are summarized in Table 2.

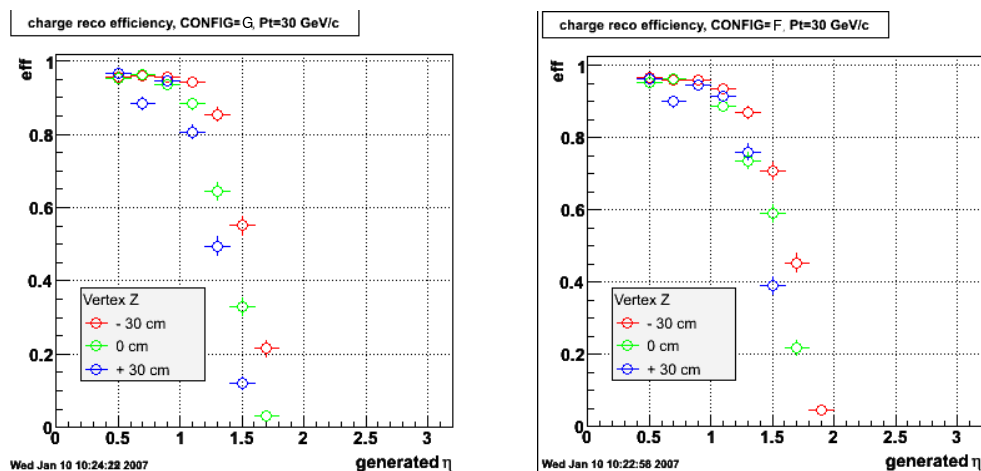


Figure 20: Charge sign discrimination probability (Ratio of the number of reconstructed tracks requiring the correct charge sign divided by the number of generated tracks) for TPC only (left) and TPC + EEMC SMD (right). In both cases a vertex constraint is taken into account.

Figure 20 shows the charge discrimination probability (Ratio of the number of reconstructed tracks requiring the correct charge sign divided by the number of generated tracks) for the case of TPC only and vertex constraint (Configuration G) and TPC, EEMC SMD and vertex constraint (Configuration F), and for the case also FGT is used (Configuration A). The TPC only case shows a clear drop in the charge discrimination probability for  $\eta > 1.5$ . The impact of the EEMC SMD can be seen comparing Configuration G and F. The need for more precise hits is clearly apparent.

Figure 21 shows on the left column the track reconstruction efficiency determined as the ratio of the number of reconstructed tracks irrespective of the correct charge sign to the number of generated tracks. The right column shows the charge sign discrimination probability determined as the ratio of the number of reconstructed tracks requiring the correct charge sign divided by the number of generated tracks. A magenta vertical line marks limit of EMC coverage in  $\eta$ . A magenta horizontal line marks 80% efficiency level. The top row shows the case for six FGT triple-GEM disks together with other tracking elements described above (Configuration A). Good track reconstruction efficiency and charge sign discrimination probability is obtained.

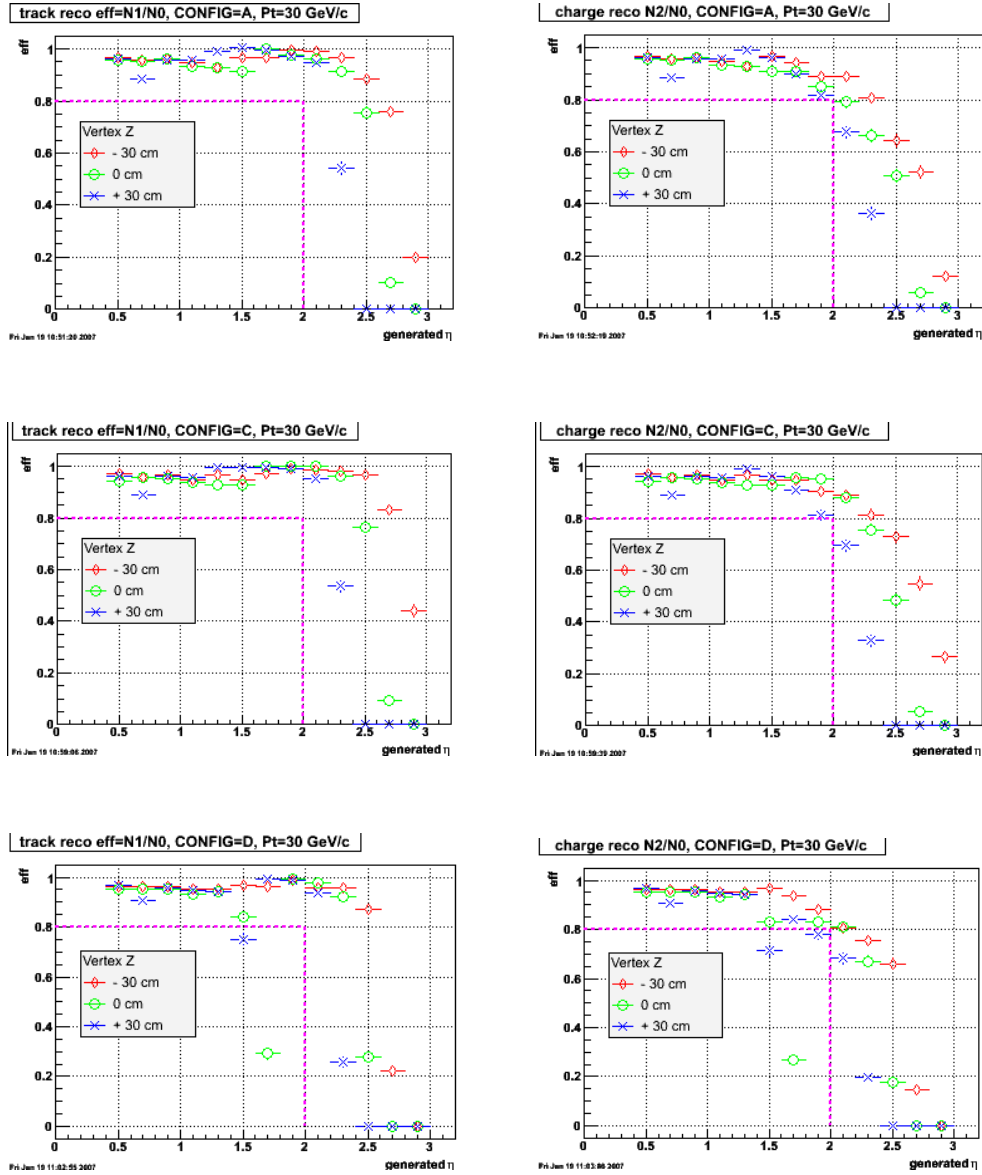


Figure 21: Track reconstruction efficiency determined as the ratio of the number of reconstructed tracks irrespective of the correct charge sign to the number of generated tracks shown on the left column. The right column shows the charge sign discrimination probability determined as the ratio of the number of reconstructed tracks requiring the correct charge sign divided by the number of generated tracks. The top panel shows the case of for six FGT triple-GEM disks together with other tracking elements described above. The middle panel refers to the case of using two additional silicon disk with an  $r - \phi$  resolution of  $20 \mu\text{m}$ . No significant improvement is obtained. The bottom panel refers to the case of using only 4 triple-GEM disks.

The middle ROW refers to the case of using two additional silicon disks with an  $r\phi$  resolution of  $20\ \mu\text{m}$  (Configuration C). No significant improvement is obtained. The bottom ROW refers to the case of using only 4 triple-GEM disks (Configuration D). The performance degrades in particular for  $\eta$  values closer to 2 AT  $Z > 0$ . Such a configuration would be the absolute minimum without any redundancy. Any further reduction of triple-GEM disks leads to a significant reduction in performance.

Figure 22 shows the change in track reconstruction efficiency and charge discrimination probability by changing the FGT resolution from  $60\ \mu\text{m}$  to  $80\ \mu\text{m}$ ,  $100\ \mu\text{m}$  to  $120\ \mu\text{m}$  (Configuration A1, A2, A3). A hit accuracy of  $70\ \mu\text{m}$  for triple-GEM detectors has been routinely obtained by various running experiments. The observed change from  $80\ \mu\text{m}$  to  $120\ \mu\text{m}$  is modest. Triple-GEM technology thus satisfies the requirements for forward tracking in STAR with a comfortable margin.

Configuration	FST	FGT (6 disks, $60\ \mu\text{m}$ )	Vertex,IST,SSD, TPC,ESMD
A	no	Default	Vtx $\sigma X = \sigma Y = 200\ \mu\text{m}$
B	2 disks, $60\ \mu\text{m}$	Default	
C	2 disks, $20\ \mu\text{m}$	Default	
D	no	4 disks	
A1	no	$80\ \mu\text{m}$	
A2	no	$100\ \mu\text{m}$	
A3	no	$120\ \mu\text{m}$	
A4	no	Default	Vtx $\sigma X = \sigma Y = 500\ \mu\text{m}$
A5	no	Default	Vtx $\sigma X = \sigma Y = 1000\ \mu\text{m}$
A6	no	Default	Vtx $\sigma Z = 30\ \text{cm}$
F	no	no	
G	no	no	no EEMC SMD hit

Table 2: *Simulation configurations. Default is A.*

The top and middle rows in Figure 23 show the track reconstruction efficiency and charge discrimination probability by changing the uncertainty of the event vertex associated to the transverse beam size from  $500\ \mu\text{m}$  to  $1000\ \mu\text{m}$  (Configuration A4 and A5). Even a change as extreme as  $1000\ \mu\text{m}$  has the effect of reducing the charge sign discrimination probability to around 70% at the highest  $\eta$  value, i.e. even in case of a poor vertex constraint, the charge sign discrimination probability is still reasonable. The bottom row in Figure 23 shows the result based on a Gaussian  $Z$  vertex distribution

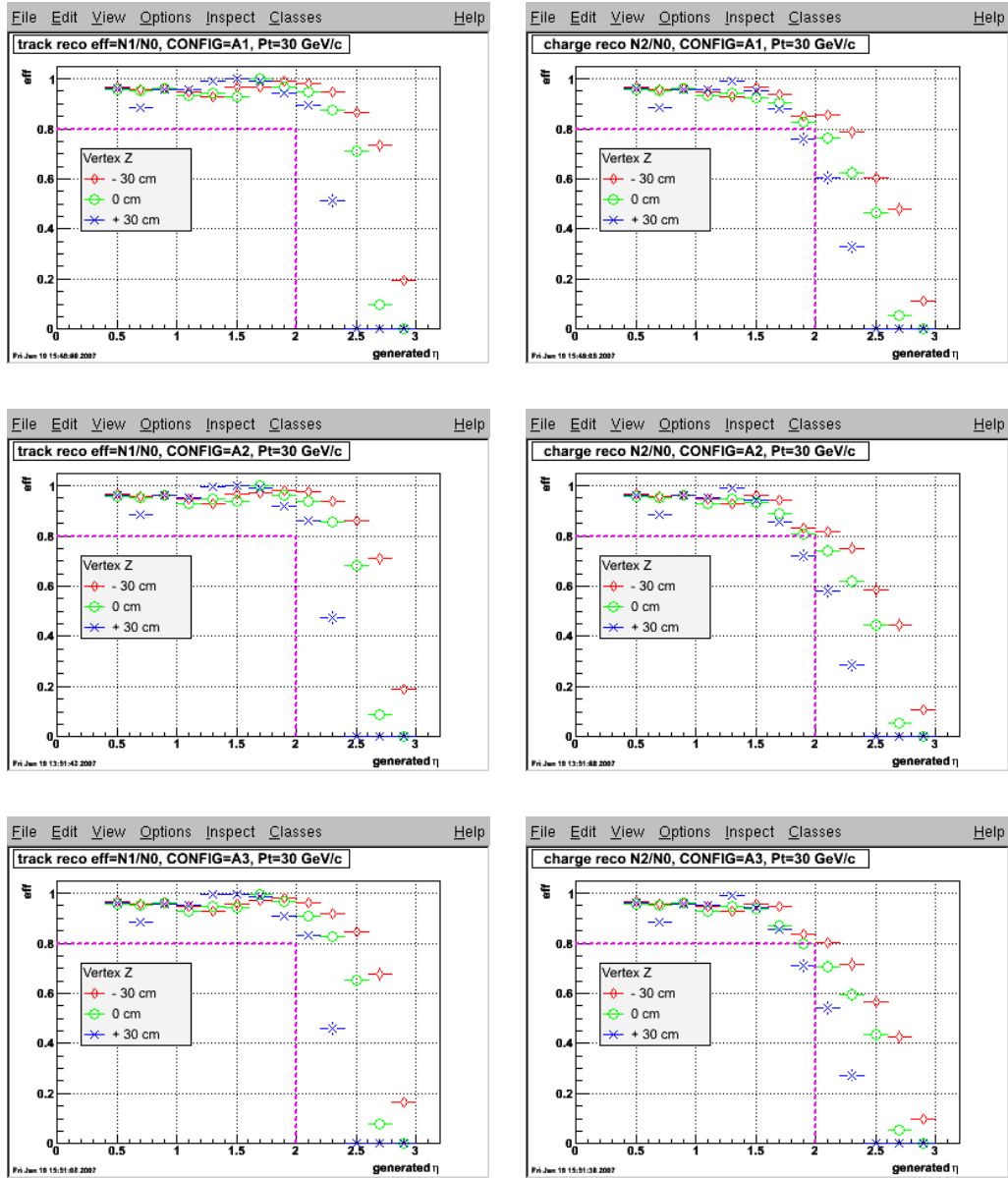


Figure 22: Track reconstruction efficiency determined as the ratio of the number of reconstructed tracks irrespective of the correct charge sign to the number of generated tracks shown on the left column. The right column shows the charge sign discrimination probability determined as the ratio of the number of reconstructed tracks requiring the correct charge sign divided by the number of generated tracks. The FGT resolution refers to  $80\ \mu\text{m}$  (top),  $100\ \mu\text{m}$  (middle) and  $120\ \mu\text{m}$  (bottom).

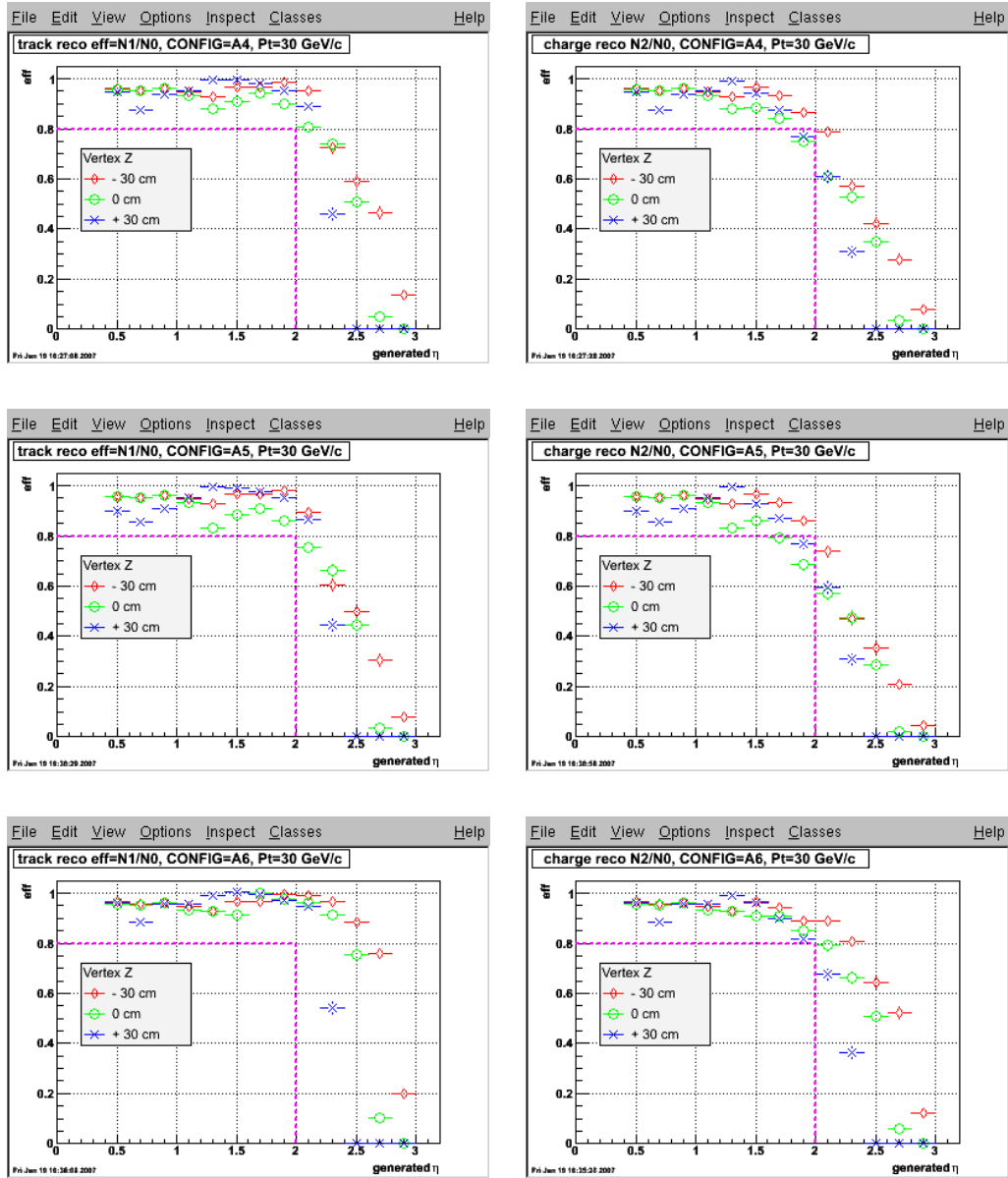


Figure 23: Track reconstruction efficiency determined as the ratio of the number of reconstructed tracks irrespective of the correct charge sign to the number of generated tracks shown on the left column. The right column shows the charge sign discrimination probability determined as the ratio of the number of reconstructed tracks requiring the correct charge sign divided by the number of generated tracks. The uncertainty of the event vertex associated to the transverse beam size has been fixed at 500  $\mu\text{m}$  (top) and 1000  $\mu\text{m}$  (middle). The bottom panel shows the case of a Gaussian Z vertex distribution with a sigma of 30 cm on top of the fixed vertex locations.

with a sigma of 30 cm on top of  $\sigma X = \sigma Y = 200\mu m$  as described above (Configuration A6). This result is consistent with configuration A.

In summary several options have been considered to provide a robust means of charge sign discrimination of high- $p_T$  tracks in the STAR EEMC acceptance region. It has been shown that this task can be accomplished using a beam line constraint, precise hit information from six triple-GEM disks, hits at forward  $\eta$  from the TPC and the electromagnetic-cluster hit information from the shower-maximum detector of the STAR EEMC. The proposed configuration based on six triple-GEM disk detectors provides optimized acceptance for a  $Z$  vertex distribution with a Gaussian distribution with a width of about 30 cm. Precise hit information from the fast inner tracking system (IST and SSD) is important to enhance the acceptance for  $Z < 0$ . The proposed configuration provides a cost effective solution based only on GEM technology. The usage of additional silicon disks at smaller radii as originally anticipated does not yield an improvement in performance and is no longer considered. All relevant aspects related to GEM technology will be discussed in the next chapter.

The remaining simulation work beyond this proposal will focus on a full W event simulation incorporating the impact of hadronic QCD background and the effect of pile-up from the TPC.

## 4 Technical realization

### 4.1 Overview

Triple-GEM disks along the beam axis are proposed for the design of the FGT. GEM technology is widely employed by current and future experiments in nuclear and particle physics. GEM trackers satisfy the requirements of the forward tracking in STAR. They are fast detectors that provide a spatial resolutions of  $70\ \mu\text{m}$  or better and can be constructed with low mass. GEM foils are routinely produced by Tech-Etch, Inc. in Plymouth, MA. The goal of the recently approved SBIR proposal by Tech-Etch Inc. in collaboration with BNL, MIT and Yale is to develop the technology at Tech-Etch for commercial production of GEM foils which meet the requirement of use in nuclear and particle physics and astrophysics research besides long-term medical imaging and homeland security applications. The focus of Phase I of the SBIR proposal is to determine the role of materials, process and post-process handling. Several prototype chambers have been assembled are currently being tested using GEM foils by Tech-Etch.

The following sections will provide an overview of the technical realization of the triple-GEM based tracking systems. The need for R&D will be clearly pointed out where necessary.

### 4.2 GEM Technology

Position sensitive detectors based on charge amplification in gases are widely used in nuclear and particle physics and are successfully applied in astrophysics, medical diagnostics and biology. Following the introduction of the multi-wire proportional chamber (MWPC) in 1968 at CERN, which has been awarded with the Nobel Prize in Physics in 1992, there has been a steady improvement in performance of these devices.

Limits in the granularity and rate capability of the MWPC lead to the development of micro-pattern gas detectors, beginning with the introduction of the micro-strip gas chamber (MSGC) in 1988. Based on the same principle as the MWPC, the use of photolithographic techniques allowed much finer structures and consequently higher granularity and higher rate capability due to fast positive ion collection.

The reduction of performance of MSGCs under sustained irradiation (aging) and damaging discharges induced for example by heavily ionizing parti-

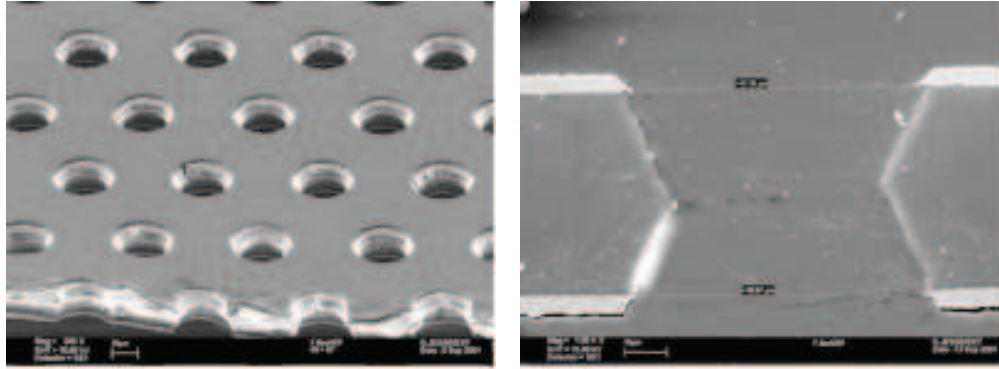


Figure 24: *Electron microscope picture of a GEM foil (left) and cross section view through one hole (right) [33].*

cles triggered new developments in the area of micro-pattern gas detectors. One of these is the Gas-Electron Multiplier (GEM), which consists of a thin metal-clad insulation foil perforated by a regular dense hole pattern [32]. The holes in the foils typically have a double conical shape with an inner diameter of  $\sim 50 \mu\text{m}$ , an outer diameter of  $\sim 70 \mu\text{m}$  and a pitch of  $140 \mu\text{m}$ . Figure 24 shows an electron microscope picture of a GEM foil and a cross section view of one hole.

A voltage difference between the two metal-clad sides of the foils leads to high electric fields in the holes, as illustrated in Figure 25. This is used to achieve electron multiplication in the detector gas.

In GEM based detectors the foil is used to amplify the charge deposited by the passage of an ionizing particle. The signal is read out on a separate readout surface. Charge transfer from the GEM to the readout is ensured by an electric field. This method has the advantage of a fast (electron only) signal due to fast positive ion collection on the GEM foils and improved discharge tolerance due to a separation of the readout and amplification stage. This separation also allows flexibility in the choice of readout geometries. Improved stability and higher gains in heavily ionizing environments is reached by cascading several GEM foils to achieve the desired gain. For the COMPASS experiment, the first large-scale application of GEM based tracking detectors, a triple GEM design was chosen [33]. The COMPASS detectors demonstrate the capabilities of GEM based detectors. A spatial resolution of  $\sim 70 \mu\text{m}$ , efficiencies in excess of 95% and a time resolution of  $\sim 12 \text{ ns}$

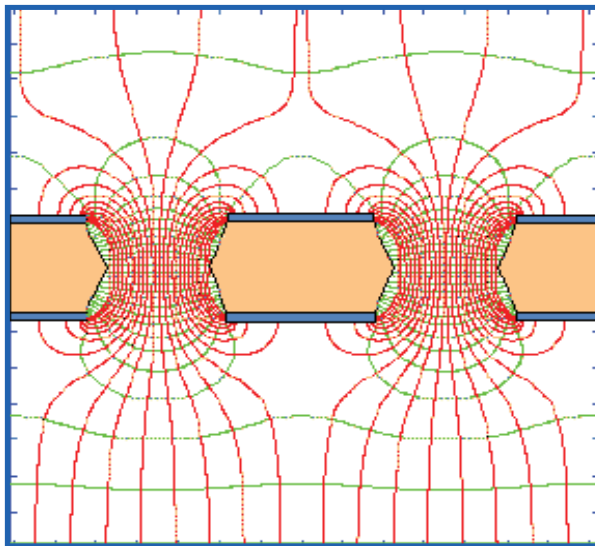


Figure 25: *Simulated electrical field inside a GEM hole. Electrons released in the upper gas volume drift into the holes, multiply and get transferred to the lower side.*

are reached in high-rate data taking [34]. In low intensity beams a spatial resolution of  $\sim 50 \mu\text{m}$  has been demonstrated. In four years of operation no electronics channel was lost. The COMPASS design also shows that GEM detectors can be built with a small material budget, an important feature for precise tracking systems. The overall thickness of the detectors is less than 0.75% of a radiation length, with a central area with a thickness of  $\sim 0.5\%$  of a radiation length [33].

GEM tracking detectors are thus a natural choice for low mass, high resolution tracking over large surface areas in high-intensity environments.

### 4.3 GEM R&D

A prerequisite for mass production of triple GEM tracking detectors is the availability of GEM foils. So far, the only source for these devices has been the CERN-EST-DEM photolithographic workshop. However, their capacity is limited and unable to meet the increasing worldwide demand for GEM foils. To address this problem a collaboration with the Plymouth, MA based company TechEtch has been formed. The development of industrial GEM

foil production is currently partially funded through the second phase of a successful SBIR proposal.

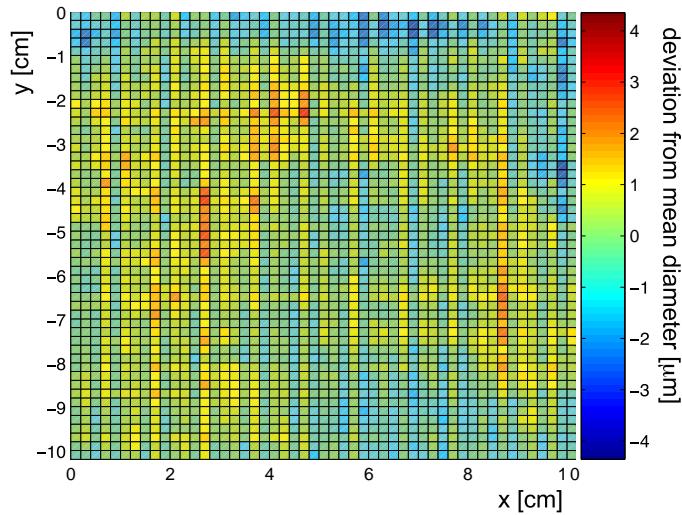


Figure 26: *Spatial homogeneity of the inner hole diameter of a Tech-Etch produced foil. The color scale (indicated on the right) shows the deviation of the inner hole diameter from the mean diameter over the whole foil.*

To evaluate GEM foils produced by Tech-Etch and perform research and development work for the STAR GEM tracker a GEM laboratory has been established at MIT and Yale University. An optical scanner was developed to measure the parameters of the foils and to test them for defects [35]. A large number of CERN and Tech-Etch produced foils has been evaluated with that scanning setup. Figure 26 shows the distribution of the inner hole diameter over the surface area of a typical  $10\text{ cm} \times 10\text{ cm}$  Tech-Etch produced GEM foil. The gain of the multiplier is strongly correlated to the inner (insulator) diameter of the holes, so a good uniformity is desirable. Tech-Etch produced foils show sufficient uniformity for the envisaged application.

A triple GEM detector prototype based on  $10\text{ cm} \times 10\text{ cm}$  GEM foils has been developed. The prototype has a two dimensional projective strip readout with  $635\text{ }\mu\text{m}$  pitch laser-etched onto a printed circuit board, and a gas-tight body made out of aluminum and plastic. The GEM foils are stretched and glued onto frames that guarantee the correct distance between foils. The high voltage to the foils is provided via a resistor network. The

detector is operated with a gas mixture of Ar:CO<sub>2</sub> 70:30.

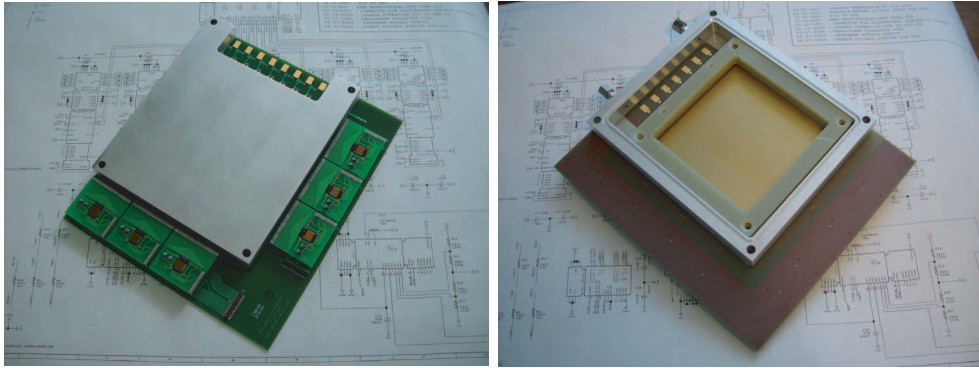


Figure 27: *Bottom (left) and top (right) view of the prototype triple-GEM chambers. The location of the sensitive detector volume can be clearly seen on the right side with the location of three inner G10 carrier frames. No GEM foils have yet been glued onto those frames. The location of groups of three readout hybrids can be clearly seen on the left side.*

Figure 27 shows a bottom and top view of the prototype triple-GEM chambers. Those chambers have been designed within the R&E laboratory. The location of the sensitive detector volume can be clearly seen on the right side of Figure 27 with the location of three inner G10 carrier frames. No GEM foils have yet been glued onto those frames. The sensitive GEM foil area amounts to  $10 \times 10\text{cm}^2$ . The bottom of this sensitive volume consists of orthogonal readout strips with a readout pitch of  $635\mu\text{m}$ . The charge induced on each individual strip is read out by a APV25-S1 readout chip which is glued and bounded onto separate readout hybrids. Each readout hybrid reads out 64 readout strips providing a total of 192 readout channels for each orthogonal direction (X/Y). The location of groups of three readout hybrids can be clearly seen on the left photograph in Figure 27.

An exploded view of the triple-GEM chamber design is shown in Figure 28. Each chamber consists of a 2D readout board which is based on a conventional printed circuit board. The 2D readout strip structure is glued on one side onto each 2D readout board. The actual triple-GEM chamber is then built up on top of this strip readout structure. This is the view of the chamber as shown on the right side in Figure 27. The connection of each readout strip to the back side which is shown on the left side in Figure 27 is

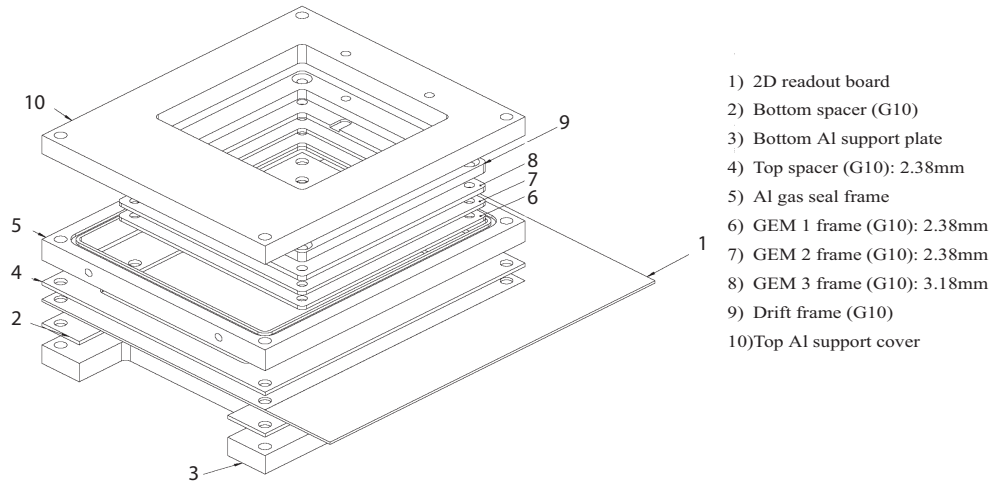


Figure 28: *Exploded view of a prototype triple-GEM chamber indicating the location of various chamber elements.*

provided through vias connections. Those are then connected to individual readout hybrids combining 64 readout strips onto one readout hybrid.

A readout system based on NIM and CAMAC electronics connected to a standard PC has been set up to read out groups of channels. First studies comparing a detector constructed with CERN made GEM foils with one based on Tech-Etch foils have been made using a low-intensity collimated  $^{55}\text{Fe}$  source (mainly 5.9 keV photons) with a rate of  $\sim 0.5 \text{ Hz/mm}^2$ . Figure 29 shows a typical spectrum recorded with the CERN foil based detector, while figure 30 shows a spectrum recorded with the detector using Tech-Etch GEM foils. The voltages were adjusted for each detector individually to use the full dynamic range of the readout system. In both the CERN and the Tech-Etch detector a clean separation of the main photo peak and the Ar escape peak is achieved. The energy resolution, defined by the ratio of the photo peak FWHM and the mean of the peak, is on the order of 20% for both detectors. The quality of the spectrum and the energy resolution is comparable to that obtained with the COMPASS triple GEM detectors [33].

By measuring the  $^{55}\text{Fe}$  pulse height in 16 different places, effectively dividing the active area in a  $4 \times 4$  grid, a map of the relative gain as a function of spatial location is obtained. Figure 31 shows the gain distribution over the

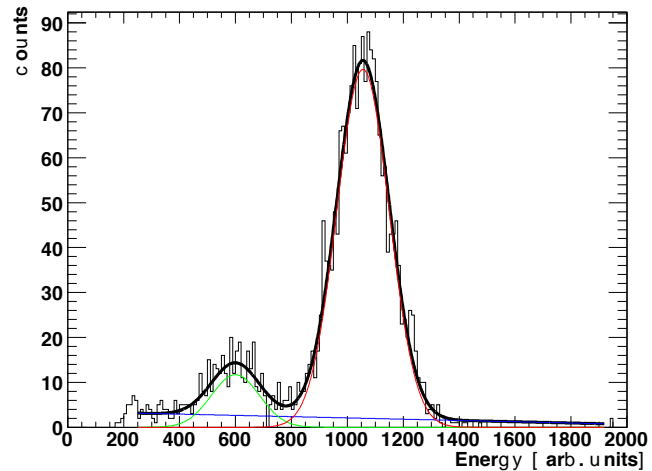


Figure 29:  $^{55}\text{Fe}$  spectrum taken with a triple GEM test detector using CERN GEM foils. The spectrum is fitted with the sum of two Gaussians and a linear background. The energy resolution (FWHM of the photo peak divided by the mean) is  $\sim 18\%$ .

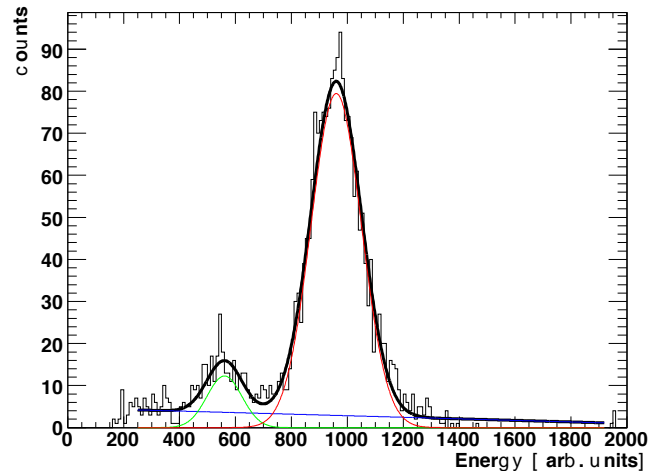


Figure 30:  $^{55}\text{Fe}$  spectrum taken with a triple GEM test detector using Tech-Etch GEM foils. The energy resolution is  $\sim 19\%$ .

10 cm  $\times$  10 cm active area of a triple GEM test detector using Tech-Etch produced GEM foils. The small RMS of the distribution of relative gain values

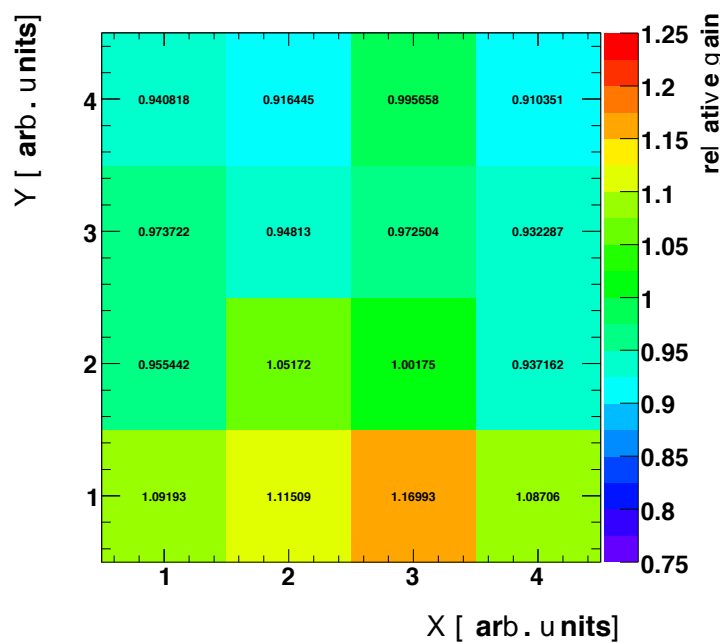


Figure 31: Map of the relative gain as a function of spatial location for a triple GEM detector using Tech-Etch produced GEM foils. The relative gain, normalized to the mean, is shown by the color scale and indicated by the numbers in each segment.

of 0.078 indicates a good uniformity of the detector. Only two out of the 16 measured gains are more than 10% off of the mean value. Similar observations were also made with a test detector using CERN produced GEM foils. These results are in line with the observations made with the COMPASS triple GEM detectors in similar measurements [33]. This demonstrates that triple GEM detectors using Tech-Etch produced foils can provide the gain homogeneity necessary for tracking detector applications.

A collaboration between TechEtch, MIT, Yale and BNL has been established to work on the optimization of the GEM foils produced by TechEtch. Foils produced under a variety of conditions using different materials are currently tested at the institutions to determine their properties, thus identifying optimal conditions and materials for the final product.

#### 4.4 Technical sub-systems

The readout electronics for the FGT are identical to the ones used for the proposed Inner Silicon Tracker IST, which is part of the inner tracking upgrade of the STAR detector. The use of one common infrastructure for both the inner and forward tracking leads to a significant reduction of the overall R&D efforts for the readout electronics for the STAR tracking upgrade.

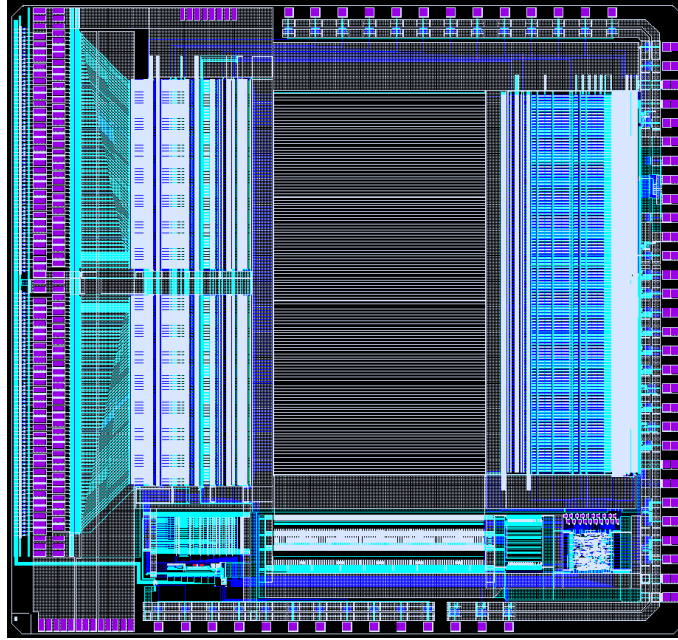


Figure 32: *Picture of the APV25-S1 die. On the left are the input pads, on the right the output pads, control pads, etcetera are visible. The whole die measures 8055 by 7100  $\mu\text{m}^2$ .*

**The APV25S1 Front-End Chip** Designing and producing a specialized readout chip for the forward tracking system is not feasible because of manpower and budget constraints. Instead a readout chip that provides the necessary functionality and was developed for another experiment will be used. The best candidate so far is the APV25-S1 readout chip which was designed for the CMS silicon tracker and of which about 75,000 will be used in CMS. An older version of that chip, the AP25-S0 is successfully used with GEM detectors in the COMPASS experiment [33]. Each channel of the APV25-S1

chip consists of a charge sensitive amplifier whose output signal is sampled at 40MHz which accounts for the LHC interaction rate. The samples are stored in a  $4\mu s$  deep analogue pipeline. Following a trigger the data in the pipeline can be processed by an analogue circuit, mainly deconvoluting the amplifier response from the actual signal and associating the signal with a certain interaction (or rather beam crossing at LHC). The resulting analogue data can then be multiplexed and send to digitizer boards. Although the analogue data leads to higher data volumes at the front-end, it is an enormous advantage that charge sharing between strips and common mode noise can be studied in detail, which will greatly improve the understanding and performance of the detector. The power consumption of the APV25-S1 is about 2 mW/channel, i.e. about 0.25 Watt/chip. The chips are fabricated in the radiation hard deep sub-micron ( $0.25\mu m$ ) process. Figure 32 shows a closeup of the APV25-S1 chip.

**Readout and DAQ Integration** Data from the 2D triple-GEM detectors are read out by the APV25-S1 readout system which consists of the following components:

- Signal Boards
- APV Module
- GEM Control Unit

The signal board collects the charge from the detector on a two dimensional strip pattern connected. The boards are fabricated from FR4 as a regular double sided 62mil PC (Printed Circuits) board which has a  $50\mu m$  thick Kapton foil glued on top which in turn is covered by  $5\mu m$  thick and  $508\mu m$  wide sensor strips on the bottom and  $5\mu m$  thick and  $127\mu m$  wide sensor strips on the top side in the case of the prototype detectors. Kapton material between top strips is removed through laser etching to uncover the bottom strips which are then gold plated. Signal strips have a  $635\mu m$  pitch. The top strips are perpendicular to the bottom strips to form a two dimensional readout board. Each signal strip is connected to the bottom side of the signal board through vias connections and to  $635\mu m$  pitch SAMTEC connectors. Those provide then the connections to the APV module. There are two sets of SAMTEC connectors, one for the X and one for the Y direction. The signal board also has two sets of an integrated bus system as part of

the communication and data collection between the APV module and GEM control unit.

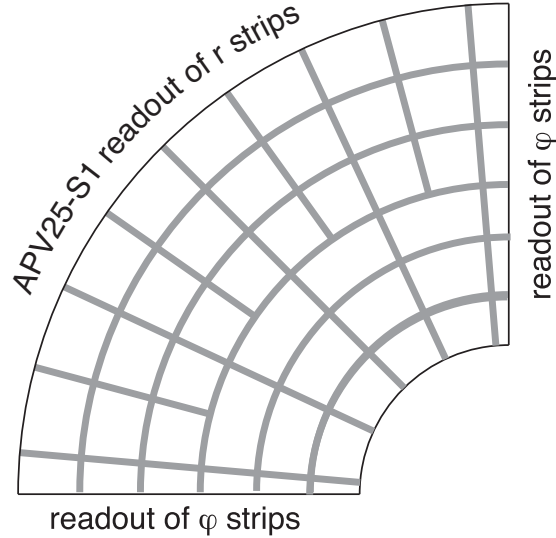


Figure 33: Schematic drawing of strip readout structure, shown for one quarter section of a triple GEM disk. The two dimensional orthogonal strip readout has coordinates in the  $r$  and the  $\varphi$  directions. The strip pitch will be around  $400 \mu\text{m}$  on both coordinates.

For the final disk design of the detectors the geometry of the readout structure has to be adapted to the detector geometry. The fabrication process of the boards will be the same as for the prototype detectors, however a lower mass construction will be used. Figure 33 shows a schematic sketch of the readout geometry of the disk detectors, using a two dimensional strip readout with strips in the  $r$  and  $\varphi$  direction. The strip pitch is around  $400 \mu\text{m}$  on both coordinates. The exact geometry and implementation of the final signal board is still under investigation. The total number of readout channels for the 6 disk FGT will be around 67 000, requiring the use of approximately 550 APV25-S1 frontend chips.

The APV module in the prototype version has an on-board glued APV25-S1 chip which is fabricated in submicron process (0.250 micron) and is connected to 68 sensor channels. There is one set of APV modules for the X-direction and a separate set for the Y-Dimension. In the prototype version of the APV modules, each APV module is connected to 68 channels. In

the final version each APV module will be connected to 128 channels and will have ADC and FIFO on board. The length of the data acquisition path will be less than 5 mm, which will guarantee minimum pickup noise. In our case, the APV25-S1 chip is operated with a clock frequency of 40MHz and read out with 20MHz. The APV25-S1 chip is set up using the I2C Philips Standard. Calibration pulses can be generated directly onboard to feed each channel.

The GEM Control Unit is the main control system for the 2D GEM readout electronics which controls all ADC, FIFO, and Data formatting and keeps communication between APV25 Modules and DAQ system. A Xilinx CPLD is the heart of each GEM Control Unit. This Xilinx component is fabricated in very deep submicron process (0.095 micron). In radiation tests which were carried out at Bates Linear Accelerator Laboratory, it was found that radiation hardness of the Xilinx CPLD component is beyond 1Mrad. The advantage of the Xilinx CPLD is based on the flexibility in re-programming to any desired configuration. Each GEM Control Unit contains for each APV25-S1 an ADC and a FIFO, where the ADC is continuously running and converting incoming signals from the APV25-S1. Upon a positive trigger decision, the data are then converted and written in parallel into all FIFOs and then in sequence from FIFO by FIFO these data are sent out in LVDS standard to the STAR DAQ system. These actions are controlled by the Xilinx CPLD device which is programmed in VHDL language. The GEM Control Unit is connected with the outside environment only through one twenty wire pairs flat ribbon cable. Each GEM Control Unit has all required voltage regulators on board. The power distribution requires therefore only one +4V power supply using one wire pair. The signal board, APV25 module and GEM control unit form one compact unit without cables and wires. All connections are realized through PC board printed layer connections. This guarantees that this system will have very low noise.

We have already made good progress in integrating the APV25 readout into the STAR environment. We have a prototype system which utilizes the STAR Trigger and Token distribution through the TCD module, and also reads out the data using an ALICE DDL link, as will be used in STAR TOF and future upgrades. This prototype system was constructed by modifying an Altera Stratix FPGA based controller, called a TCPU, developed for the STAR Time of Flight, and by adding some interfacing for the MIT GEM controller, and other systems such as I2C for the APV25, and Canbus for the Stratix TCPU board.

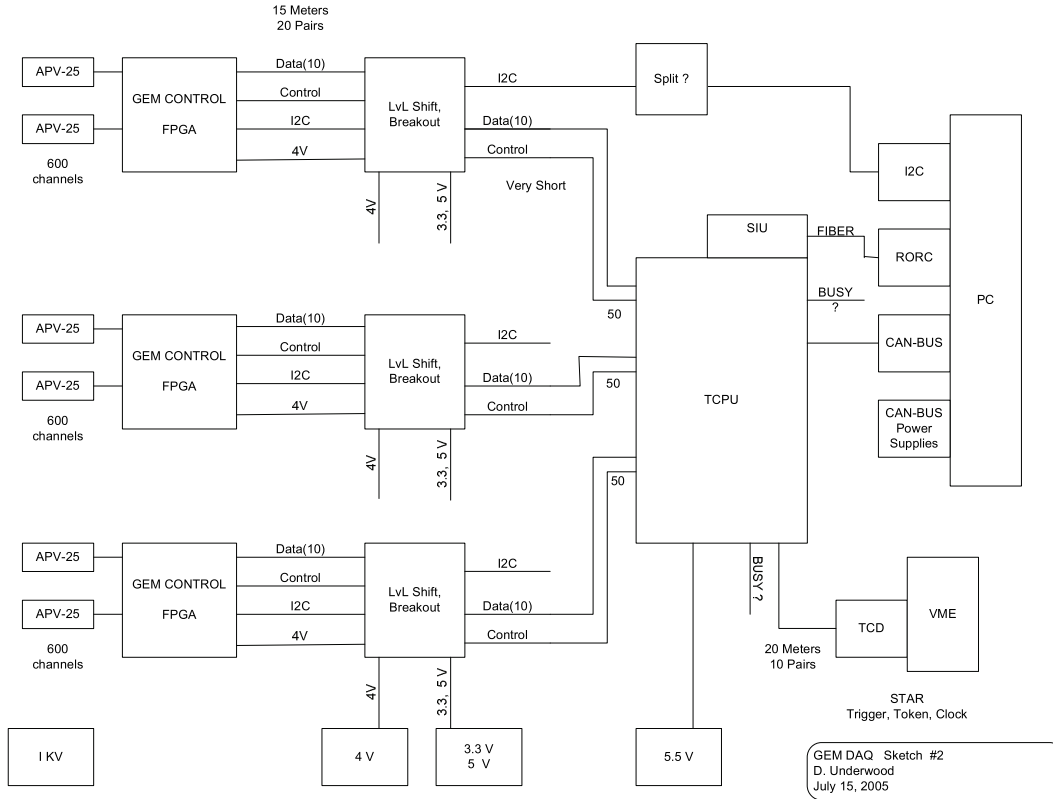


Figure 34: *Sketch of the APV25 chip readout system and STAR DAQ integration.*

The prototype system, shown schematically in Figure 34, was successfully tested with a small resistive plate chamber with cosmic muons. Figure 35 shows one of the events recorded with that setup. The signals in the RPC are much wider than they will be in GEM detectors since the signal pick-up is inductive compared to direct electron collection in a triple GEM device. RPC signals are also much higher, apparent from the fact that most channels reach saturation. While the charge of a RPC signal is typically between 0.2 pC and 2 pC, a MIP signal in a triple GEM detector is around 10 fC. Nevertheless, these results demonstrate that the full readout chain from the front-end chip to the data acquisition is working as expected.

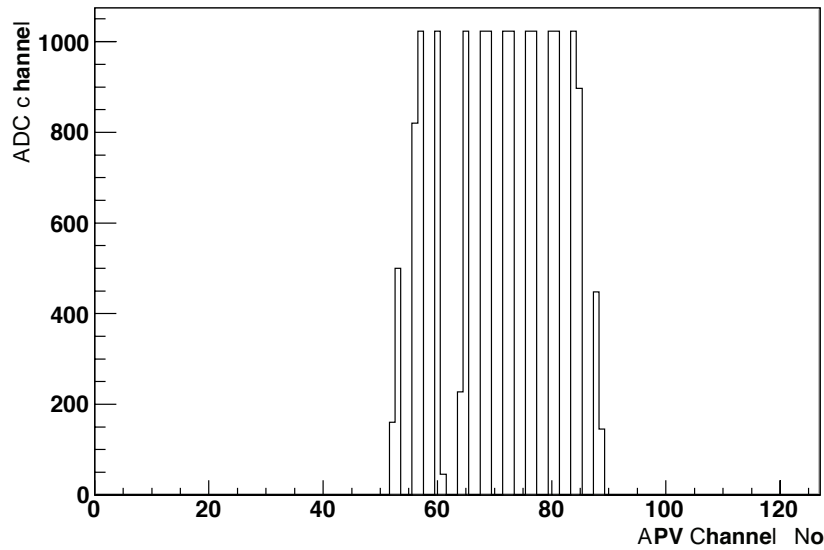


Figure 35: *Cosmic muon pulse in a small RPC recorded with the APV25S1 chip and the full DAQ chain. The two on – two off structure is due to the connection scheme of the APV chip, where only half of the channels are connected to readout strips.*

For tests with a small number of detectors in a low rate environment a USB based readout system for the APV25 and GEM Control Unit is currently being developed. This system allows to install test setups at several locations at low cost, and will be used for GEM detector tests with cosmic muons. The DAQ software for this system is based on LabView and can be run on a standard PC or laptop computer.

**High-voltage and low-voltage system** Considering the standard requirements both for the high voltage and low voltage system, those can likely be obtained as almost off the shelf components. Since these systems will be located relatively close to the detector there is the need for remote control and monitoring. Companies like Wiener can build these systems to the desired specifications, including a CANBUS interface.

**Slow control systems** A slow control system has to measure all working parameters of the intermediate and forward tracker. The temperature of the hybrids and the currents and voltages of the components on the hybrids need to be monitored continuously. Also temperatures, gas flow rates and dry air flow rates need to be recorded regularly. Preferably all these monitoring values get entered into a database. In case that the parameters get out of predefined operating values alarms should be send to the shift crew.

Although STAR is using EPICS as its standard slow control system there is a slight preference to use LabView instead. Labview provides the user with virtually any instrument driver and a very convenient user interface. LabView runs on both Windows and Linux. It is relatively simple to interface LabView and EPICS. However, at the moment, both options are still open.

**Support structure** The support structure of the forward GEM tracker should be both mechanically stable and low mass. The amount of material in this structure will for a large part determine how its performance will be affected by non-desired processes like multiple scattering, conversions, delta rays and nuclear interactions. On the other hand it has to provide a mechanically and thermally stable support for the detector elements. To make it possible to carry out maintenance work and to accommodate a possible staged installation schedule, the structure also has to be highly modular.

The mechanical support structure should be made with an overall accuracy of  $100\mu\text{m}$ , which is about the best accuracy which can be achieved for mechanical structures of this size. This overall accuracy will be sufficient to assemble the different parts of the system. Trying to improve on this accuracy would immediately drive up the cost.

The structure should also be thermally sound. It is not foreseen that the detector will be operated other than at room temperature, both during lab testing and while installed in STAR. However, there is always the chance of thermal excursions and the structure should be able to handle those. Preferably the thermal expansion coefficient should be zero. Where this can not be achieved, there should be enough slack to take up the expansion to avoid putting stress on components. For instance, sensor ladders can be mounted only rigidly on one side while the other side is seated in sapphire mounts which make longitudinal expansion possible. Also special care should be taken in the choice of adhesives and avoiding 'bimetal' effects during construction of the parts. The whole structure has to be stiff enough to retain the surveyed

positions after installation in the STAR magnet.

A structure made out of carbon fiber composites currently seems the most promising choice. Many groups are using this material to build highly accurate trackers. There is substantial experience, e.g. among the LHC experiments, that we can rely on when designing and building such a complex structure. It is clear that significant R&D is necessary to achieve a low mass system. It is not clear at the present time if there are sufficient resources within STAR available to achieve this. Another option is to outsource the design to the industry as it is foreseen for the PHENIX forward silicon upgrade.

**Installation procedures** It is foreseen to assemble the complete tracking system including a new beam pipe outside, e.g. in the STAR experimental hall. This should include a system test using a cosmic ray test setup. This would also allow to test the integration into the STAR DAQ system at the same time. This step has been proven by many experiments as a critical step for a successful operation after installation. After completion of a complete system test, the new tracking system including a new beam pipe would be then installed as one unit inside STAR.

## References

- [1] D. de Florian, G.A. Navarro and R. Sassot, *Phys. Rev. D* 71, 094018 (2005).
- [2] Nadolsky P.M. and Yuan C.-P., *Nucl. Phys.* B666 (2003) 3.
- [3] S. Vidor, 'The RHIC Spin Program: Snapshots of progress', Invited talk at the 13<sup>th</sup> International Symposium on High-Energy Spin Physics (SPIN98), Provino, Russia.
- [4] G. Bunce et., *Ann. Rev. Nucl. Part. Sci.* 50 (2000) 525.
- [5] Ashman J, et al [European Muon Collaboration (EMC)]. *Phys. Lett.* B206 (1988) 364; *Nucl. Phys.* B328 (1989) 1; Adeva B, et al [Spin Muon Collaboration (SMC)]. *Phys. Rev. D* 58 (1998) 112001; Anthony PL, et al (E142 Collaboration). *Phys. Rev. D* 54 (1996) 6620; Abe K, et al (E143 Collaboration). *Phys. Rev. D* 58 (1998) 112003; Abe K, et al (E154 Collaboration). *Phys. Rev. Lett.* 79 (1997) 26; Anthony PL, et al (E155 Collaboration). *Phys. Lett.* B463 (1999) 339; Ackerstaff K, et al (HERMES Collaboration). *Phys. Lett.* B404 (1997) 383; Airapetian A, et al. *Phys. Lett.* B442 (1998) 484; for review, see Hughes E, Voss R. *Ann. Rev. Nucl. Part. Sci.* 49 (1999) 303.
- [6] Anselmino M, Efremov A, Leader E. *Phys. Rep.* 261 (1995) 1; (E) 281 (1997) 399; Cheng HY. *Int. J. Mod. Phys.* A11 (1996) 5109; hep-ph/0002157; Lampe B, Reya E. *Phys. Rep.* 332 (2000) 1; S. Bass, *Eur. Phys. J.* A5 (1999) 17.
- [7] Lipkin HJ. *Phys. Lett.* B256 (1991) 284; *Phys. Lett.* B337 (1994) 157; Lichtenstedt J, Lipkin HJ. *Phys. Lett.* B353 (1995) 119.
- [8] Glück M, Reya E, Stratmann M, Vogelsang W. *Phys. Rev. D* 53:(191)996) 4775.
- [9] Amaudruz P, et al (NMC). *Phys. Rev. Lett.* 66 (1991) 2712; Arneodo M, et al (EMC). *Phys. Rev. D* 50 (1994) 1.
- [10] Baldit A, et al (NA51 Collaboration). *Phys. Lett.* 332 (1994) 244; Hawker EA, et al (E866 Collaboration). *Phys. Rev. Lett.* 80 (1998) 3715.

- [11] Ackerstaff K, et al (HERMES Collaboration). *Phys. Rev. Lett.* 25 (1998) 5519.
- [12] B. Dressler et al., *Eur. Phys. J.* C18 (2001) 719; B. Dressler et al., *Eur. Phys. J.* C14 (2000) 147.
- [13] Adeva B, et al (SMC). *Phys. Lett.* B420 (1998) 180; Ackerstaff K, et al (HERMES Collaboration). *Phys. Lett.* B464 (1999) 123.
- [14] Craigie NS, Hidaka K, Jacob M, Renard FM. *Phys. Rep.* 99 (1983) 69; Bourrely C, Soffer J, Leader E. *Phys. Rep.* 59 (1980) 95.
- [15] Bourrely C, Soffer J. *Phys. Lett.* B314 (1993) 132; *Nucl. Phys.* B423 (1994) 329; Chiappetta P, Soffer J. *Phys. Lett.* B152 (1985) 126.
- [16] Bourrely C, Soffer J. *Nucl. Phys.* B44 (1995) 5341.
- [17] Kamal B. *Phys. Rev. D* 57 (1998) 6663.
- [18] Gehrmann T. *Nucl. Phys.* B534 (1998) 21.
- [19] Bland LC. Presented at Circum-Pan-Pacific RIKEN Symp. High Energy Spin Phys. (Pacific Spin 99), Wako, Jpn., Nov. 1999. hep-ex/0002061 (2000)
- [20] Gehrmann T, Stirling WJ. *Phys. Rev. D* 53:( (191)996) 6100.
- [21] Sjostrand T. *Comput. Phys. Commun.* 82 (1994) 74.
- [22] Balazs C, Yuan C.-P. *Phys. Rev. D* 56 (1997) 5558.
- [23] Abe F, et al (CDF Collaboration). *Phys. Rev. Lett.* 74 (1995) 850; *Phys. Rev. Lett.* 81 (1998) 5754.
- [24] Gottfried K. *Phys. Rev. Lett.* 18 (1967) 1174.
- [25] CTEQ Collaboration, Lai HL, et al. *Phys. Rev. D* 55 (1997) 1280.
- [26] Martin AD, Roberts RG, Stirling WJ, Thorne RS. *Eur. Phys. J.* C14 (2000) 133.
- [27] Vogelsang W. et al. *Phys. Rev. D* 63 (2001) 094005.

- [28] STAR collaboration, Heavy-Flavor Tracker proposal, Internal document.
- [29] STAR collaboration, Intermediate Tracker proposal, Internal document.
- [30] B. Surrow, EPJdirect C2 (1999) 1.
- [31] W. Fischer, private communications.
- [32] F. Sauli, *Nucl. Instr. and Meth.* A386 (1997) 531.
- [33] C. Altunbas et al., *Nucl. Instr. and Meth.* A490 (2002) 177.
- [34] B. Ketzer et al., *Nucl. Instr. and Meth.* A535 (2004) 314.
- [35] U. Becker et al., *Nucl. Instr. and Meth.* A556 (2006) 527.